# Universidad San Francisco de Quito

## Colegio de Posgrados

## Exploring Seismo-Electromagnetic Influences on Cosmic Ray Detection

Tesis en torno a una hipótesis o problema de investigación

James Alexander Peñafiel Labanda

Edgar Carrera, Ph.D. Director de Trabajo de Titulación

Trabajo de titulación de posgrado presentado como requisito para la obtención del título de Magíster en Física

Quito, Ecuador

# Universidad San Francisco de Quito Colegio de Posgrados

# HOJA DE APROBACIÓN DE TRABAJO DE TITULACIÓN

## Exploring Seismo-Electromagnetic Influences on Cosmic Ray Detection

### James Alexander Peñafiel Labanda

Nombre del Director de Programa:

Título académico:

Director del programa de:

Dario Niebieskikwiat

Doctor en Física

Maestría en Física

Nombre del Decano del Colegio Académico: Eduardo Alba Título académico: Doctor en Ciencias Matemáticas Decano del Colegio: Colegio de Ciencias e Ingeniería

Nombre del Decano del Colegio de Posgrados: Dario Niebieskikwiat Título académico: Doctor en Física

Quito, diciembre 2024

## Derechos de Autor

Por medio del presente documento certifico que he leído todas las Políticas y Manuales de la Universidad San Francisco de Quito USFQ, incluyendo la Política de Propiedad Intelectual USFQ, y estoy de acuerdo con su contenido, por lo que los derechos de propiedad intelectual del presente trabajo quedan sujetos a lo dispuesto en esas Políticas.

Asimismo, autorizo a la USFQ para que realice la digitalización y publicación de este trabajo en el repositorio virtual, de conformidad a lo dispuesto en la Ley Orgánica de Educación Superior del Ecuador.

Nombre completo: James Alexander Peñafiel Labanda

Código: 00334876

Cédula de indentidad: 0951701978

Lugar y fecha: Quito, 12 de diciembre del 2024

# Aclaración para publicación

Nota: El presente trabajo, en su totalidad o cualquiera de sus partes, no debe ser considerado como una publicación, incluso a pesar de estar disponible sin restricciones a través de un repositorio institucional. Esta declaración se alinea con las prácticas y recomendaciones presentadas por el Committee on Publication Ethics COPE descritas por Barbour et al. (2017) Discussion document on best practice for issues around theses publishing, disponible en http://bit.ly/COPETheses.

# Unpublished Document

Note: The following capstone project is available through Universidad San Francisco de Quito USFQ institutional repository. Nonetheless, this project – in whole or in part – should not be considered a publication. This statement follows the recommendations presented by the Committee on Publication Ethics COPE described by Barbour et al. (2017) Discussion document on best practice for issues around theses publishing available on http://bit.ly/COPETheses.

# Dedicatoria

A mis padres, por su amor y apoyo incondicional.

## Agradecimientos

Quiero expresar mi agradecimiento a mis padres por su apoyo incondicional, sin el cual este trabajo no habría sido posible. A mi tutor y director de tesis, Edgar Carrera, por su orientación constante y dedicación durante todo el proceso de elaboración de este trabajo. Mi agradecimiento también al Departamento de Física, cuyo entorno académico y profesional ha sido fundamental para mi desarrollo a lo largo de la maestría. Finalmente, quiero reconocer al personal de la Dirección de la Maestría por su constante apoyo y por el compromiso con la excelencia académica, que han sido clave en mi éxito durante este programa de posgrado.

#### Resumen

Este estudio investiga la influencia de las variaciones geo-electromagnéticas inducidas sísmicamente en los flujos de rayos cósmicos secundarios, con el objetivo de determinar si dichos efectos pueden ser detectados a nivel de suelo. Utilizando herramientas avanzadas de simulación, específicamente CORSIKA y Geant4, el estudio asume que las variaciones geo-electromagnéticas podrían influir en los flujos de rayos cósmicos secundarios y evalúa su detectabilidad. CORSIKA se utilizó para simular las lluvias aéreas extensivas (EAS) generadas por la interacción de los rayos cósmicos primarios con la atmósfera hasta una cierta altitud. Desde ese punto, las partículas secundarias fueron propagadas en Geant4, donde se introdujeron las variaciones de campos geo-electromagnéticos para modelar su posible influencia sobre el flujo. Los resultados de la simulación no mostraron desviaciones detectables en el flujo de rayos cósmicos secundarios a nivel del suelo, incluso al probar una amplia gama de intensidades de campos eléctricos y magnéticos. Estos hallazgos sugieren que, al menos bajo las configuraciones probadas, las perturbaciones geo-electromagnéticas no inducen cambios medibles en el flujo de rayos cósmicos secundarios. El estudio también resalta los desafíos computacionales encontrados durante el proceso de simulación, subrayando la importancia de optimizar los parámetros de simulación para cumplir con las demandas computacionales a gran escala. Trabajos futuros podrían centrarse en perfeccionar los modelos de simulación e incorporar condiciones atmosféricas más realistas para comprender mejor el impacto de las perturbaciones geo-electromagnéticas en los flujos de rayos cósmicos secundarios.

Palabras clave: Rayos cósmicos secundarios, variaciones geo-electromagnéticas, lluvias aéreas extensivas (EAS), CORSIKA, Geant4, campos eléctricos y magnéticos.

### Abstract

This study investigates the influence of seismic-induced geo-electromagnetic field variations on secondary cosmic ray fluxes, focusing on whether such effects can be detected at ground-level. Using advanced simulation tools, specifically CORSIKA and Geant4, the study assumes that geo-electromagnetic variations might influence secondary cosmic ray fluxes and evaluates their detectability. CORSIKA was employed to simulate the extensive air showers (EAS) generated by primary cosmic rays interacting with the atmosphere up to a certain altitude. From that point, the secondary particles were propagated in Geant4, where geo-electromagnetic field variations were introduced to model their potential influence on the flux. The simulation results showed no detectable deviations in the secondary cosmic ray flux at ground level, even when testing a wide range of electric and magnetic field strengths. These findings suggest that, at least under the configurations tested, geo-electromagnetic disturbances do not induce measurable changes in secondary cosmic ray flux. The study also highlights the computational challenges encountered during the simulation process, emphasizing the importance of optimizing simulation parameters to meet the large-scale computational demands. Future work could focus on refining simulation models and incorporating more realistic atmospheric conditions to better understand the potential impact of geo-electromagnetic disturbances on secondary cosmic ray fluxes.

**Keywords:** Secondary cosmic rays, geo-electromagnetic variations, extensive air showers (EAS), CORSIKA, Geant4, electric and magnetic fields.

# Contents

1	Introduction			12
2	Literature review			
	2.1	Cosmi	ic Rays and Extensive Air Showers	14
		2.1.1	Showers initiated by a photon or electron	
		2.1.2	Showers initiated by a hadron	
	2.2	Electr	comagnetic Variations, Cosmic Rays, and Their Potential Con-	
			on to Seismic Activity	19
	2.3		riew of Simulation Tools	
3	Met	hod		22
J	3.1		egy for the study	
	3.2		ation Framework and Setup	
	3.3		ation of Extensive Air Showers (EAS) in CORSIKA	
	0.0	3.3.1	CORSIKA overview	
		3.3.2	Automated Simulation Setup for EAS Studies Using ARTI	
	3.4	Atmos	spheric model in Geant4	
		3.4.1	Simulation Volume	
		3.4.2	Material Definition	
		3.4.3	Particle Injection	
		3.4.4	Interaction Physics	
	3.5	Conta	inerization Workflow Using Docker	
		3.5.1	Docker Implementation in the Simulation Framework	34
	3.6	Comp	outational Resources and Environment Setup	
		3.6.1	Parallelization and Scalability	36
		3.6.2	Data Storage and Management	
		3.6.3	Cost Optimization	
	3.7	Uncer	tainty Analysis	37
		3.7.1	Statistical Uncertainties	37
4	Res	ults aı	nd Discussions	40
	4.1	Validation of the Simulation Framework		
	4.2	Uncertainty Quantification for Geo-Electro-		
			etic Influences	43
	4.3	_	et of Geo-electromagnetic Variations	
		4.3.1	Validation of Geo-Electromagnetic Field Implementation	44
		4.3.2	Analysis of Geo-Electromagnetic Field Effects on Secondary	
			Cosmic Ray Flux	46
	4.4	Simula	ation Framework Computational Challenges and Solutions	47

5 Conclusions 51

# List of Figures

2.1 2.2 2.3 2.4	Longitudinal development of the air shower [15]	15 16 16 17
3.1	Schematic representation of the atmospheric simulation model in Geant 4. The parallelepiped represents the simulation world, with key dimensions and parameters: $\mathbf{H}$ (vertical extent of the simulation), $\mathbf{D}$ (horizontal width and length), $\mathbf{h}$ (height of the Zone of Influence), $\mathbf{r}$ (radius of the Zone of Influence), and $\mathbf{d}$ (horizontal distance between the detector and the Zone of Influence). The lower boundary of the simulation represents the altitude of Cumbayá, Quito (2200 m above sea level), while the upper boundary is set at $2200 + \mathbf{H}$ . The detector, located 5 km along the negative $y$ -axis, measures the secondary particle flux ( $\Phi_g$ ) within a 1 km $\times$ 1 km area. The Zone of Influence is where geo-electromagnetic variations are introduced to study their effects on particle propagation	. 24
3.2	Coordinate system from the CORSIKA manual, with the origin defined at $(0,0,\mathrm{OBSLEV})$ , where OBSLEV corresponds to the observation level altitude. The z-axis points upward, the x-axis points north, and the y-axis points west. Particle momentum is represented by the angles $\Theta$ (zenith angle) and $\Phi$ (azimuthal angle) [16]. Note: The $\Phi$ angle shown here is unrelated to the $\Phi_t$ , $\Phi_c$ , and $\Phi_g$ flux parameters used in this study	25
4.1 4.2	Visualization of the electric field and geometry in Geant 4 Particle flux as a function of distance for different magnetic field strengths (2.84e-5 T, 1e-7 T, 1e-5 T, 1e-3 T). The uncertainty in	45
4.3	the flux is represented by error bars."	48
	error bars.	40

# Chapter 1

# Introduction

Cosmic rays, high-energy particles originating from outer space, interact with Earth's atmosphere to produce extensive air showers (EAS). These cascades of secondary particles, detectable at ground level, provide critical insights into high-energy astrophysics and atmospheric processes. The study of EAS is essential for understanding the propagation and interaction of cosmic rays as they traverse the atmosphere.

Several studies have documented electromagnetic anomalies preceding seismic events, suggesting a coupling between tectonic stress and variations in Earth's magnetic and electric fields. For instance, Moore (1964) [31] observed significant geomagnetic disturbances near fault zones, attributed to piezomagnetic effects induced by stress in the Earth's crust. Similarly, Davis and Johnston (1983) [9] and Masci et al. (2009) [29] reported localized geomagnetic anomalies near moderate earthquakes, often linked to tectonic stress and crustal magnetization changes. Other research, such as Takla et al. (2011) [38] and Gao et al. (2014) [13], identified combined magnetic and electric field disturbances near seismic events, further supporting the hypothesis of tectonic influences on localized electromagnetic fields.

P. Homola et al. (2023) [19] explored the potential link between secondary cosmic ray fluxes and seismic effects. Their findings suggest a correlation between cosmic ray flux variations and global seismic events. While the direct relationship between cosmic ray flux variations and seismic phenomena remains uncertain, this hypothesis indicates that cosmic rays might be sensitive to the electromagnetic disturbances associated with tectonic activity. However, such correlations have yet to be established at a local scale, leaving an open question about their detectability in specific regions.

Given the evidence of geo-electromagnetic variations associated with seismic phenomena and the potential sensitivity of secondary cosmic rays to these disturbances, this study focuses on the detectability of such effects. Using advanced simulation frameworks like CORSIKA [16] and Geant4 [1], the work assumes that geo-electromagnetic variations might influence secondary cosmic ray fluxes and seeks to determine if such changes could be observed at ground-level detectors. By simulating various configurations, this study lays the groundwork for understanding whether localized electromagnetic effects could leave a detectable signature in secondary cosmic ray observations, without speculating on their origins or mechanisms.

This thesis is structured into five chapters. Chapter 1 provides an introduction to the motivations, objectives, and scope of this research. Chapter 2 explores the nature of cosmic rays and extensive air showers, discussing their generation, propagation, and interactions within the Earth's atmosphere, as well as their relevance to seismic studies. Chapter 3 outlines the methodology, detailing the development of a Geant4-based atmospheric model, the integration of CORSIKA data for secondary particle injection, and the implementation of localized electromagnetic fields to simulate seismic-induced variations. Chapter 4 presents the results and analysis, focusing on the impact of geo-electromagnetic disturbances on secondary cosmic ray fluxes and their implications for earthquake precursor detection. Finally, Chapter 5 concludes with a summary of the findings, their contributions to geophysical research, and suggestions for future work in this interdisciplinary field.

### **Objectives**

### General Objective

To evaluate the impact of seismic-induced geo-electromagnetic field variations on the flux of secondary cosmic rays at ground level, using advanced simulation tools to determine measurable variations under controlled conditions.

### Specific Objectives

- 1. **To construct** a simplified atmospheric model in Geant4 to simulate the propagation of secondary cosmic rays under varied electromagnetic field conditions.
- 2. **To integrate** secondary particle data generated with CORSIKA into the Geant4 simulations, in order to replicate realistic cosmic ray interactions within the Earth's atmosphere.
- 3. **To analyze** the changes in secondary cosmic ray flux at ground level caused by localized variations in geo-electromagnetic fields, using cloud-based computational resources for efficient simulation and data processing.

# Chapter 2

# Literature review

This chapter introduces the fundamental concepts and theoretical framework necessary for this study. Section 2.1 explores the phenomenon of cosmic rays and extensive air showers (EAS), examining their origins, propagation, and key characteristics. Section 2.2 discusses the electromagnetic variations associated with seismic activity and their potential connection to cosmic rays, based on previous studies documenting geomagnetic and electric field anomalies. Finally, Section 2.3 provides an overview of the simulation tools employed in this work, highlighting their roles in modeling cosmic ray interactions and analyzing the potential effects of geo-electromagnetic disturbances on secondary cosmic ray fluxes.

### 2.1 Cosmic Rays and Extensive Air Showers

The study of Extensive Air Showers (EAS) plays a fundamental role in understanding the interactions between high-energy cosmic rays and the Earth's atmosphere. These phenomena occur when high-energy primary hadronic cosmic rays, with energies greater than  $10^{13}$  eV (or 10 TeV), enter the atmosphere isotropically from outer space and collide with atmospheric atoms, primarily oxygen  $(O_2)$ , nitrogen  $(N_2)$ , and argon (Ar) [21]. During these interactions, what matters most is not the distance traveled by the particles along their path, but the amount of matter they traverse, which is intrinsically linked to the density of the medium. The air density varies with altitude, which affects the propagation of the particles. The atmospheric depth X, measured in units of  $g/cm^2$ , quantifies the amount of material the particles pass through. The first interaction of the primary cosmic rays with the atmosphere occurs at a depth known as  $X_0$ , typically found between 10 and 40 km above sea level, in the upper troposphere or stratosphere [22].

In the longitudinal development of the air shower, the number of secondary particles initially increases exponentially, reaching a maximum value  $X_{\text{max}}$ , after which it decreases as the particles lose energy. This process is depicted in Figure 2.1, which shows the longitudinal development of an extensive air shower through the atmosphere [15]. During this stage, new particles are produced, many of them unstable, which then cause further interactions. As the shower progresses, the secondary particles lose energy, and some processes are disabled due to energy thresholds required for certain interactions. In Figure 2.2, the longitudinal profile of a moderately inclined air shower is shown, illustrating the curvature of the shower front and the distribution of particles in a thin disk near ground level. When using a ground-level

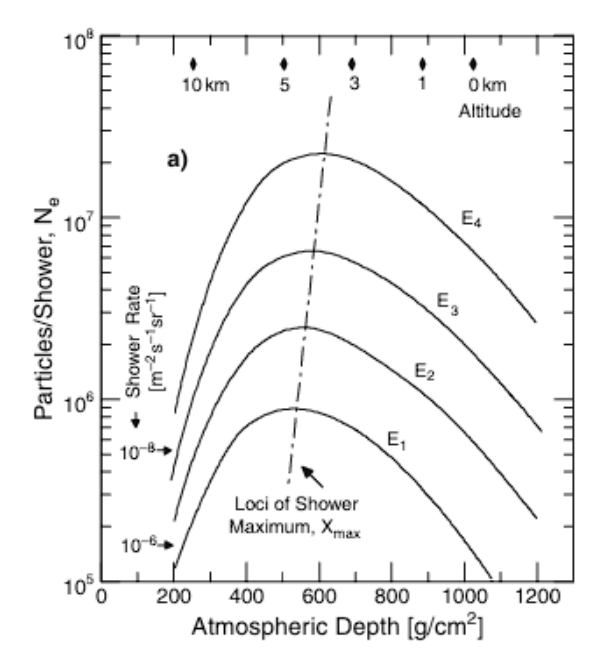


Figure 2.1: Longitudinal development of the air shower [15].

detector array, this profile allows us to infer the direction of the primary cosmic ray. The detectors closest to the shower's axis will trigger first, while those further from the axis will activate later. By analyzing the time differences in the detector activations, we can reconstruct the direction of the primary particle's trajectory. Additionally, the number of secondary particles detected by each detector provides further information about the nature of the primary cosmic ray, as a higher particle density can suggest a more energetic primary, and the distribution pattern can help identify whether the primary was proton, or heavier nucleus.

The evolution of these showers also depends on the nature of the primary particle. For example, in the case of photons, the dominant interactions are electromagnetic, while protons and nuclei are primarily governed by hadronic interactions.

Figure 2.3 shows the zenith angle distribution of the rate of air showers at mountain altitudes and sea level, illustrating how the inclination of the shower affects the secondary particle distribution and the rate of occurrence.

The behavior of cosmic rays is also influenced by their energy spectrum. Figure 2.4 presents the energy spectrum of cosmic rays with energies above  $10^{11}$  eV. This spectrum follows a smooth power-law distribution with three main features: the "cosmic ray knee" around  $10^{15}$  eV, the "ankle" at about  $3 \times 10^{18}$  eV, and the cutoff at  $3 \times 10^{19}$  eV. The decrease in cosmic ray intensity with increasing energy means that high-energy cosmic rays are difficult to measure directly using experiments on balloons and satellites. To measure these high-energy rays, large-area air shower arrays larger than  $10^4$  m² are required [27].

The secondary shower generated by these interactions is classified into three main components: the electromagnetic cascade (EM), composed of photons, electrons, and positrons, and which is the most dominant component, accounting for nearly 99% of the energy in the shower; the hadronic cascade, formed by the interaction of primary and secondary hadrons; and the muonic cascade, which results from the decay of unstable particles like pions and kaons. The dominant interactions in each

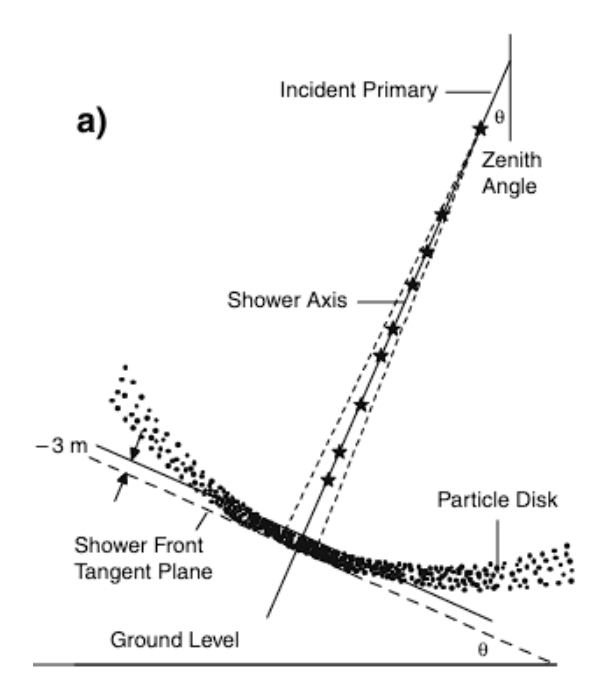


Figure 2.2: Longitudinal profile of an air shower [15].

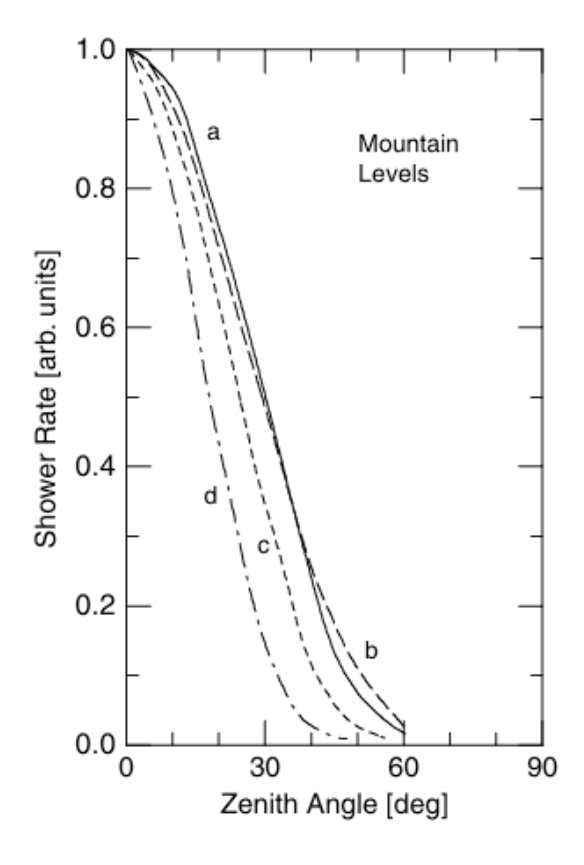


Figure 2.3: Zenith angle distribution [15].

type of shower depend on the primary particle's nature, and analyzing the differences in the development of these three components provides valuable information about the energy and composition of the primary cosmic ray [3].

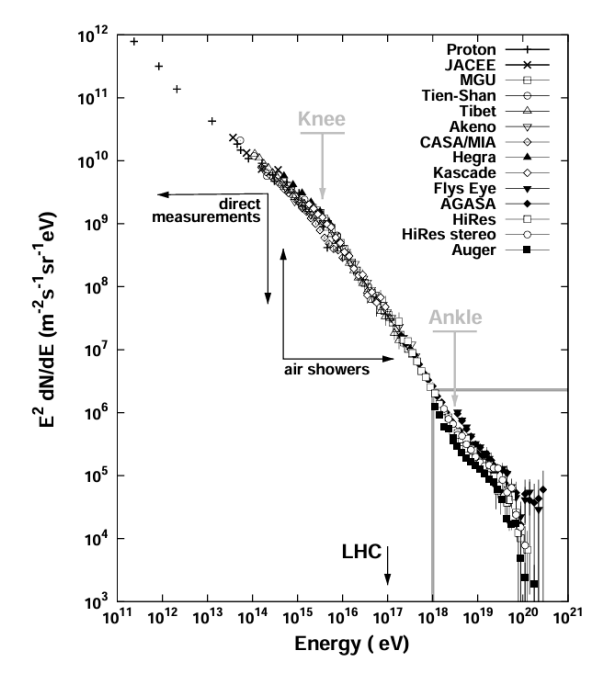


Figure 2.4: Differential energy spectrum of cosmic rays of energy above  $10^{11}$  eV multiplied by  $E^2$ . [27].

#### 2.1.1 Showers initiated by a photon or electron

Air showers, or extensive air showers (EAS), consist of three main components: the hadronic, electromagnetic, and muonic components. Approximately 99% of the particles in these showers belong to the electromagnetic component, which also contains around 90% of the energy of the primary particle. This component includes photons, electrons, and positrons and is generally referred to as the EM component [3].

The development of a shower initiated by a photon or an electron (where "electron" refers to both positive and negative charges) is primarily governed by electromagnetic processes. The two main interaction channels for electromagnetic cascades are Bremsstrahlung and pair production in the atmosphere. For a given air nucleus, with charge Z and atomic number A, the corresponding reactions are:

- Bremsstrahlung (Bremsstrahlung radiation): This process occurs when an electron or positron is decelerated by the electromagnetic field of the nucleus, emitting a photon.
- Pair production: High-energy photons can interact with the electromagnetic field of a nucleus to produce an electron-positron pair.

Bremsstrahlung: 
$$e \xrightarrow{\frac{A}{Z}Y} e\gamma$$
Pair production:  $\gamma \xrightarrow{\frac{A}{Z}Y} e^+e^-$ 
(2.1)

These processes are closely coupled. Photons with sufficient energy can create pairs, which in turn undergo Bremsstrahlung, producing more photons. This coupling of the reactions is the main reason for the formation of the EM cascade.

The behavior of an electromagnetic cascade was first described by Heitler [18], who proposed a simplified model. According to Heitler, when a primary particle interacts with the atmosphere at a given height, it first splits into two particles with equal energy, each carrying half of the primary particle's energy. These particles then split into four, with one-quarter of the primary energy, and so on. After a certain number of interactions, the number of particles grows exponentially, with  $2^n$  particles.

Heitler further suggested that the cascade continues to develop until the particles reach a critical energy  $E_C$ , at which point the number of particles no longer increases, and the maximum number of particles in the cascade is determined by the ratio  $\frac{E_0}{E_C}$ , where  $E_0$  is the energy of the primary particle.

The maximum depth of the cascade, or the point at which the particle number ceases to grow, is given by the following relation:

$$X_{\text{max}} = \log_2\left(\frac{E_0}{E_C}\right) \tag{2.2}$$

This equation describes the development of an electromagnetic cascade initiated by a photon or electron and serves as a simplified model of the actual cascade process. Despite its simplicity, Heitler's model provides a clear understanding of the general behavior of electromagnetic cascades and their evolution in the atmosphere. For hadron-initiated cascades, similar principles apply, though the exact details of the process may vary due to hadronic interactions.

### 2.1.2 Showers initiated by a hadron

Hadronic showers begin when high-energy hadrons, such as protons or heavy nuclei, interact with atmospheric nuclei, primarily oxygen  $(O_2)$ , nitrogen  $(N_2)$ , and argon (Ar). These interactions generate a cascade of secondary particles, including both charged and neutral pions. In the upper atmosphere, neutral pions  $(\pi^0)$  typically decay into photons and electrons, which contribute to the electromagnetic (EM) component of the shower. The relevant reaction is as follows [33, 15].

$$\pi^{0} \to \gamma \gamma \ [98.8\%]$$
 $\pi^{0} \to \gamma e^{+}e^{-} \ [1.2\%]$ 
(2.3)

In contrast, charged pions ( $\pi^+$  and  $\pi^-$ ) decay into high-energy muons, which make up the muonic component of the shower. This muonic component is much more significant in hadronic showers compared to electromagnetic showers, making muons a key signature of hadronic interactions. The decay processes of charged pions are.

$$\pi^+ \to \mu^+ \nu_\mu \ [99.99\%]$$
  
 $\pi^+ \to e^+ \nu_e \ [0.01\%]$  (2.4)

Strange mesons, primarily kaons, also contribute to the muonic component of the shower. Kaons decay into muons through the reaction in 2.5, and these muons can continue to decay into more muons. The last of these muons may trigger a secondary electromagnetic shower, which further develops into new generations of particles.

$$K^{+} \to \mu^{+} \nu_{\mu} \quad [63.43\%]$$

$$K^{+} \to \pi^{+} \pi^{0} \quad [21.13\%]$$

$$K^{+} \to \pi^{+} \pi^{+} \pi^{-} \quad [5.6\%]$$

$$K^{+} \to \pi^{0} e^{+} \nu_{e} \quad [4.9\%]$$

$$(2.5)$$

The relatively long lifetime of muons, combined with relativistic time dilation effects, makes them highly detectable and an important part of understanding the initial hadronic interactions. Muons also experience significant radiative effects due to their high energy, leading to large fluctuations in the energy of secondary particles. This radiation causes the production of secondary electromagnetic showers through muon pair production, as in 2.6, and may also produce hadronic sub-cascades due to muon interactions with the medium, as in 2.7.

$$\mu^{\pm} \xrightarrow{\frac{A}{Z}Y} \mu^{\pm} e^{+} e^{-} \tag{2.6}$$

$$\mu^{\pm} \xrightarrow{\frac{A}{Z}Y} \mu^{\pm} + \text{hadrones}$$
 (2.7)

Heitler's model of particle cascades can be applied to hadronic showers, with the key parameter being the hadronic interaction length  $\lambda_I$  [30, 36]. At each step of the cascade, with a thickness of  $\lambda_I \ln 2$ , hadronic interactions produce  $2N_{\pi}$  charged pions and  $N_{\pi^0}$  neutral pions. The neutral pions decay immediately, contributing to the electromagnetic component, while the charged pions continue to interact and decay into muons.

The cascade continues to evolve, with each interaction step contributing to the electromagnetic component. As charged pions reach the critical energy  $E_{\pi c}$ , they decay into muons instead of interacting further. About one-third of the pion energy goes into the electromagnetic component, while the rest remains in hadrons. The longer it takes for pions to reach  $E_{\pi c}$ , the larger the electromagnetic contribution becomes. This means that in longer showers, the muons from pion decay will have lower energy.

Moreover, the critical energy  $E_{\pi c}$  increases with altitude due to variations in atmospheric density. As a result, showers at higher altitudes will produce fewer muons than those near sea level. This altitude dependence emphasizes the importance of accurate atmospheric models in simulating hadronic showers and understanding cosmic ray interactions [27].

# 2.2 Electromagnetic Variations, Cosmic Rays, and Their Potential Connection to Seismic Activity

The relationship between electromagnetic variations and seismic activity has been extensively studied, providing a robust framework for understanding physical processes occurring during the earthquake preparation phase. Research into the phenomenon of earthquake lights (EQL)—luminous events observed near seismic zones

proposed that tectonic stress could release radon gas, ionizing the near-surface atmosphere and increasing atmospheric conductivity. This process was thought to trigger electromagnetic discharges that manifest as visible lights [28].

Subsequent investigations expanded on these findings, demonstrating that seismic events can induce anomalies in geomagnetic fields, particularly in the ultra-low frequency (ULF) range. For example, significant perturbations in the geomagnetic vertical component were identified prior to seismic events, attributed to piezomagnetic and electrokinetic effects [31, 38]. Similarly, localized geomagnetic anomalies observed along active fault zones were associated with stress-induced piezomagnetic changes within close proximity of the fault lines [9].

Recent studies have also identified negative atmospheric electric field anomalies prior to major seismic events. These anomalies, attributed to increased geopotential in stressed crustal regions, were observed under clear weather conditions and have been described as similar to "underground lightning" [37]. These findings highlight the complex coupling between tectonic stress and the electromagnetic environment.

Cosmic ray studies have also intersected with this area of research, exploring how variations in geo-electromagnetic fields might influence cosmic ray propagation and detection. For instance, significant decreases in cosmic ray scalar rates have been observed coinciding with the arrival of seismic waves, suggesting a potential influence of localized geo-electromagnetic disturbances on cosmic ray flux modulation [2]. Additionally, investigations into galactic cosmic ray (GCR) flux variations during solar cycles have shown correlations between GCR intensity, atmospheric pressure changes, and seismic activity, suggesting indirect links mediated by solar-terrestrial interactions [32].

The Earth's magnetic field also plays a significant role in cosmic ray propagation. Studies have demonstrated that magnetic fields alter the lateral spread of high-energy electrons in extensive air showers (EAS), emphasizing the importance of considering geomagnetic variations in cosmic ray analyses [4]. This effect is particularly relevant in regions with active seismicity, where dynamic field variations may further modulate secondary particle behavior.

This study does not aim to investigate or propose the use of electromagnetic or cosmic ray anomalies as direct seismic precursors. Instead, it focuses on evaluating whether localized geo-electromagnetic variations associated with seismic activity can significantly alter the flux of secondary cosmic rays at ground level. By employing advanced simulation frameworks such as CORSIKA [17] and Geant4 [1], this study explores the interaction between particle physics and geophysical processes, contributing to the broader understanding of how geo-electromagnetic fields influence secondary cosmic ray propagation.

#### 2.3 Overview of Simulation Tools

In previous sections, we discussed cosmic rays, extensive air showers (EAS), and their potential link to seismic activity. To further investigate these phenomena, it is essential to model the interactions between high-energy cosmic rays and the Earth's atmosphere, as this allows us to better understand the processes underlying EAS formation and the role that geo-electromagnetic variations may play in modulating cosmic ray flux. This project utilizes a simulation framework that integrates several key tools to study cosmic ray interactions and the effects of geo-electromagnetic per-

turbations on secondary cosmic ray fluxes. The ARTI framework [35], developed by the Latin American Giant Observatory (LAGO) [26], automates the configuration and execution of simulations for cosmic ray studies, providing a standardized setup for simulation runs. This framework uses CORSIKA (COsmic Ray SImulations for KAscade) to model the primary cosmic ray interactions and the generation of secondary particles. These particles are then propagated through the atmosphere using Geant4, a powerful toolkit for simulating the passage of particles through matter.

The primary objective of this project is to use these simulation tools to study the behavior of secondary particles produced by cosmic rays under standard conditions and in the presence of geo-electromagnetic variations induced by seismic activity. By combining the capabilities of ARTI, CORSIKA, and Geant4, this framework allows for a comprehensive analysis of cosmic ray interactions, helping to understand how these particles propagate through the atmosphere and how local geo-electromagnetic perturbations might influence the secondary cosmic ray flux detected at ground level.

Through these simulations, the project aims to identify and analyze the potential impact of seismic-induced anomalies on the cosmic ray flux, contributing to the broader field of cosmic ray research and atmospheric science.

# Chapter 3

# Method

This chapter presents the methodology used to analyze the impact of seismic-induced geo-electromagnetic field variations on secondary cosmic ray fluxes. Section 3.1 introduces the overall strategy for the study, explaining the approach to simulating and analyzing the effects of geo-electromagnetic variations on secondary cosmic ray fluxes. Section 3.2 introduces the overall simulation framework, emphasizing the integration of CORSIKA [17] and Geant4 [1] for modeling secondary particle fluxes and their propagation. Section3.3 focuses on CORSIKA simulations and the ARTI framework, detailing the processes for simulating extensive air showers (EAS) and automating parameter configurations. Section 3.4 describes the implementation of the atmospheric model in Geant4, including the definition of subvolumes, material properties, and the methodology for particle injection. Section 3.5 highlights the containerization workflow using Docker, ensuring portability and reproducibility of the simulation setup. Finally, Section 3.6 outlines the computational resources and cloud infrastructure employed, specifically the use of Google Cloud Platform (GCP) for parallelization and scalable execution of the simulation workflow.

### 3.1 Strategy for the study

This study aims to explore the potential influence of seismic-induced geo-electromagnetic field variations on the flux of secondary cosmic rays, also known as extensive air showers (EAS), at ground level. These secondary particles are generated when primary cosmic rays interact with atmospheric nuclei, initiating a cascade of secondary particles that propagate through the atmosphere and reach the Earth's surface.

The approach involves simulating two scenarios: the first evaluates the flux of secondary cosmic rays at ground level without the presence of any electric or magnetic fields, while the second incorporates geo-electromagnetic field variations associated with seismic activity. By comparing the particle fluxes observed in these scenarios, this study seeks to determine whether such variations could induce detectable changes in the secondary cosmic ray flux.

To implement this strategy, two simulation frameworks are used in conjunction. CORSIKA [17] is employed to model the secondary cosmic rays produced by the interaction of primary cosmic rays with atmospheric nuclei. This simulation tracks the development of extensive air showers until the particles reach a specific altitude above sea level. At this point, the secondary particles are collected and propagated through Geant4 [1], which allows for the inclusion of a localized region representing

a geo-electromagnetic variation induced by seismic activity. This dual-framework approach ensures a detailed and accurate analysis of the potential effects of geo-electromagnetic fields on secondary cosmic rays.

### 3.2 Simulation Framework and Setup

This section introduces the simulation framework designed to analyze the potential influence of seismic-induced geo-electromagnetic field variations on secondary cosmic ray flux at ground level. The framework integrates two distinct tools: CORSIKA, used to simulate secondary cosmic ray flux under standard atmospheric conditions, and Geant4, which models particle propagation within an atmospheric representation under varying electric and magnetic fields.

The Geant4 atmospheric model, illustrated in Figure 3.1, is structured as a parallelepiped and defined by the parameters  $\mathbf{H}$ ,  $\mathbf{D}$ ,  $\mathbf{h}$ ,  $\mathbf{r}$ , and  $\mathbf{d}$ . The lower boundary of this model represents the altitude of Cumbayá, Quito (approximately 2200 m above sea level), while the upper boundary extends to  $2200 + \mathbf{H}$ . It is important to clarify that, within the Geant4 framework, these boundaries serve as abstract representations for the simulation geometry; no explicit altitudes are physically modeled. The parameter  $\mathbf{H}$  defines the vertical extent of the Geant4 simulation world, and  $\mathbf{D}$  specifies the width and length of the parallelepiped.

Within this simulation world, the Zone of Influence is modeled as a cylindrical region characterized by its height  $(\mathbf{h})$  and radius  $(\mathbf{r})$ . This Zone of Influence is where localized electromagnetic field variations are applied to simulate potential seismic-induced anomalies. The parameter  $\mathbf{d}$  defines the horizontal distance between the Zone of Influence and a detector, which is located at the lower boundary of the simulation world. This spatial configuration is specifically designed to enable the analysis of how varying distances affect the observed secondary particle flux.

In this study, analyzing secondary particle fluxes is central to understanding cosmic ray behavior under different conditions. The fluxes of interest include  $\Phi_t$ ,  $\Phi_q$ , and  $\Phi_c$ , each playing a distinct role in the simulation process.

 $\Phi_t$  represents the secondary particle flux obtained from CORSIKA simulations at an altitude of 2200 meters above sea level. CORSIKA provides a detailed simulation of extensive air showers over a large area; however, only particles within a specific region are considered for this study. This region is defined as a square area with dimensions of  $1 \, \mathrm{km} \times 1 \, \mathrm{km}$ , centered at a point located 5 km along the negative y-axis relative to the origin of the CORSIKA coordinate system, as illustrated in Figure 3.2. The origin of the coordinate system,  $(0,0,\mathrm{OBSLEV})$ , represents the reference observation altitude of the simulation.

On the other hand, in the Geant4 simulation, a detector volume is explicitly constructed at the lower boundary of the parallelepiped model to represent the same area as defined in CORSIKA simulation. The detector has identical spatial characteristics to the selected region in CORSIKA: a square area of  $1 \,\mathrm{km} \times 1 \,\mathrm{km}$ , centered at a point located 5 km along the negative y-axis. This detector in Geant4 measures the secondary particle flux  $\Phi_g$ , which corresponds to the flux of particles detected at the lower boundary under the simulation conditions implemented in Geant4. The comparison between  $\Phi_t$  and  $\Phi_g$  serves as an essential validation step, ensuring that Geant4 can accurately reproduce particle fluxes under standard conditions before introducing any geo-electromagnetic variations in the Zone of Influence.

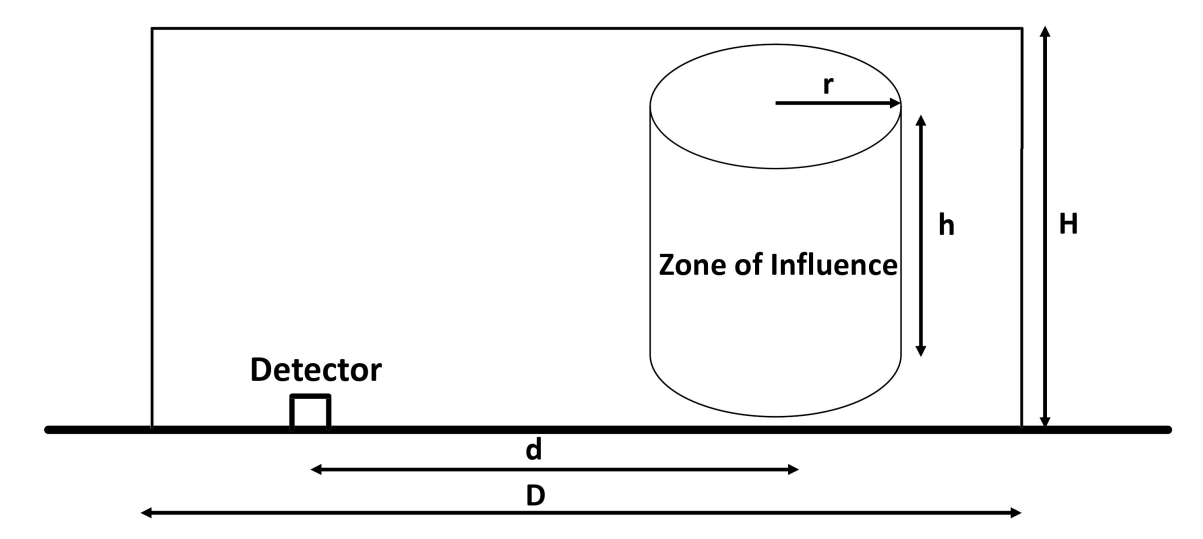


Figure 3.1: Schematic representation of the atmospheric simulation model in Geant4. The parallelepiped represents the simulation world, with key dimensions and parameters:  $\mathbf{H}$  (vertical extent of the simulation),  $\mathbf{D}$  (horizontal width and length),  $\mathbf{h}$  (height of the Zone of Influence),  $\mathbf{r}$  (radius of the Zone of Influence), and  $\mathbf{d}$  (horizontal distance between the detector and the Zone of Influence). The lower boundary of the simulation represents the altitude of Cumbayá, Quito (2200 m above sea level), while the upper boundary is set at  $2200 + \mathbf{H}$ . The detector, located 5 km along the negative y-axis, measures the secondary particle flux ( $\Phi_g$ ) within a 1 km  $\times$  1 km area. The Zone of Influence is where geo-electromagnetic variations are introduced to study their effects on particle propagation.

Lastly, the secondary particle flux  $\Phi_c$  is defined based on the output of CORSIKA simulations at an altitude of  $2200 + \mathbf{H}$  meters. Unlike  $\Phi_t$ , which is confined to a specific localized area,  $\Phi_c$  encompasses the total flux of secondary particles across the entire simulation area provided by CORSIKA, without any spatial restrictions. This flux is used as the input for initializing particle propagation in Geant4.

#### Simulation workflow

The simulation workflow begins with CORSIKA simulations that generate both  $\Phi_t$  and  $\Phi_c$ . These fluxes are essential for two purposes:  $\Phi_t$  is used to validate  $\Phi_g$  from Geant4, while  $\Phi_c$  serves as the source for particle injection in the Geant4 simulation. Within Geant4,  $\Phi_c$  is injected at the upper boundary of the simulation world, allowing particles to propagate through the atmospheric model toward the detector at the lower boundary. This setup enables a thorough evaluation of how secondary cosmic ray fluxes at ground level are influenced by localized geo-electromagnetic field variations, providing insights into the potential impact of seismic-induced anomalies on particle detection.

#### Summary of key simulation components

• **H:** Vertical height of the **Geant4** world, representing the distance between the lower boundary (Cumbayá, Quito at 2200 m) and the upper boundary (2200 + **H**).

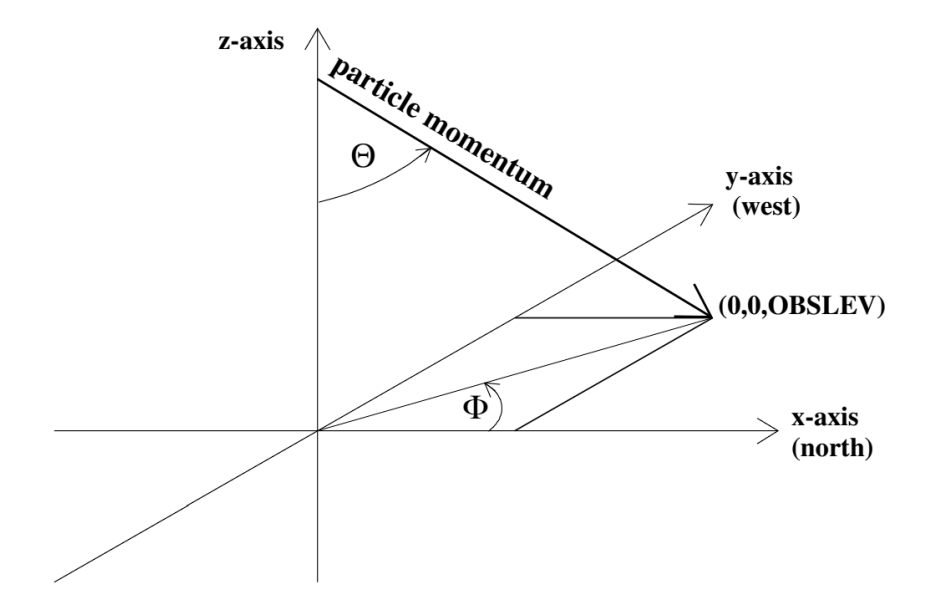


Figure 3.2: Coordinate system from the CORSIKA manual, with the origin defined at  $(0,0,\mathrm{OBSLEV})$ , where OBSLEV corresponds to the observation level altitude. The z-axis points upward, the x-axis points north, and the y-axis points west. Particle momentum is represented by the angles  $\Theta$  (zenith angle) and  $\Phi$  (azimuthal angle) [16]. Note: The  $\Phi$  angle shown here is unrelated to the  $\Phi_t$ ,  $\Phi_c$ , and  $\Phi_g$  flux parameters used in this study.

- **D:** Width and length of the **Geant4** world, defining the horizontal dimensions of the parallelepiped simulation area.
- d: Horizontal distance between the Zone of Influence and the center of the detector in the Geant4 world.
- h: Height of the Zone of Influence, representing the vertical extent of the cylindrical region where localized geo-electromagnetic field variations are introduced.
- r: Radius of the Zone of Influence.
- $\Phi_t$ : Secondary particle flux provided by CORSIKA at 2200 m altitude, measured over a localized area of 1 km × 1 km, centered at 5 km along the negative y-axis.
- $\Phi_g$ : Secondary particle flux measured at the detector in Geant4, located at the lower boundary (2200 m), over an area of  $1 \text{ km} \times 1 \text{ km}$ .
- $\Phi_c$ : Secondary particle flux at the upper boundary (2200 + **H**), encompassing all particles across the entire simulation area provided by CORSIKA, used as the input for the Geant4 simulation.

# 3.3 Simulation of Extensive Air Showers (EAS) in CORSIKA

The first step in the simulation framework involves the use of CORSIKA, a widely recognized software for modeling the interaction of primary cosmic rays with the Earth's atmosphere. As the foundational component of the methodology, CORSIKA simulates extensive air showers produced by cosmic ray interactions in atmospheric layers, providing detailed information about the resulting secondary particles. These simulations are essential for defining particle fluxes at specific altitudes, which are then used as input for the Geant4 simulations described in Section 3.4.

#### 3.3.1 CORSIKA overview

CORSIKA (COsmic Ray Simulations for KAscade) is a sophisticated Monte Carlo program designed to simulate the evolution of extensive air showers (EAS) in the atmosphere. Initiated by photons, protons, nuclei, or other particles, these simulations allow for detailed studies of particle cascades.

For this study, the CORSIKA v7.7402 version was utilized, configured through the ARTI framework to ensure consistency and automation in the simulation setup. The following options and modules were specifically employed:

- **High-energy hadronic interactions:** QGSJET-II04. This model is used to simulate the interactions of high-energy cosmic ray particles with the atmosphere, accounting for the production of secondary particles in collisions between these cosmic rays and atmospheric nuclei. It is particularly suited for describing interactions at very high energies.
- Low-energy hadronic interactions: GHEISHA-2002. This module focuses on lower-energy interactions, handling collisions involving particles such as neutrons and protons with atmospheric nuclei. It uses data from experiments to simulate these interactions, ensuring accurate modeling for energies below 80 GeV.
- Electromagnetic interactions: EGS4. This module simulates electromagnetic processes such as bremsstrahlung and pair production, which are critical for understanding the behavior of electrons, positrons, and photons in extensive air showers.
- Atmospheric modeling: Curved atmospheric model and external atmospheric modules. These configurations provide a realistic representation of the atmosphere, incorporating variations in density and altitude.
- Flux calculations: Configured for a volumetric detector to account for secondary particle distributions.

These configurations were chosen to ensure realistic and accurate simulations of secondary cosmic ray interactions under the specified atmospheric conditions. For further details on the physics and options implemented in CORSIKA, refer to the official physics description manual [17].

# 3.3.2 Automated Simulation Setup for EAS Studies Using ARTI

#### S0 Stage in ARTI: Primary Simulation Setup

The ARTI framework, as previously discussed in Chapter 2, Section 2.3, is organized into several stages, with the S0 stage responsible for preparing input files and running initial configurations for simulations in CORSIKA. This stage is crucial, as it sets up all the necessary parameters and generates the required files for CORSIKA to simulate extensive air showers (EAS) created by cosmic ray interactions in the atmosphere.

During the S0 stage, ARTI produces the following files:

- 60 CORSIKA steering files (\*.input), which contain specific instructions for each simulation.
- 60 bzip2-compressed binary files (DAT\*.bz2), storing all simulated EAS information generated by CORSIKA.
- 60 bzip2-compressed output files (\*.lst.bz2), capturing the output logs produced by CORSIKA during each simulation run.

The script used to initiate this stage is do\_sims.sh, a script developed within the ARTI framework and available in the LAGO GitHub repository [8]. This script accepts various options to control the simulation parameters, and for this project, it was executed with the following command:

In this command:

- theta and thetamax: Represent the minimum and maximum zenith angles, defining the range of angles at which primary particles enter the atmosphere. For this study, the range of angles was set from 0 to 90 degrees.
- time: Specifies the simulation duration, which was configured to 600 seconds.
- -i: Sets the energy of the primary particles, which in this case is configured to 10,000 GeV.
- -y: Specifies the volumetric detector mode.

This configuration causes ARTI to simulate the flux of primary particles as they arrive at the Earth's atmosphere at an altitude of 112 km a.s.l. Using the specified input parameters, ARTI models the primary cosmic ray flux over a defined area, integrating over energy and solid angle ranges. It then calculates the expected number of primary particles for each element type (ranging from protons to iron, i.e.,  $1 \le Z \le 26$ ), using the equation:

$$\Phi(E_p, Z, A, \Omega) \simeq j_0(Z, A) \left(\frac{E_p}{E_0}\right)^{\alpha(E_p, Z, A)}$$
(3.1)

where  $\Phi(E_p, Z, A, \Omega)$  represents the flux as a function of primary energy  $(E_p)$ , atomic number (Z), atomic mass (A), and solid angle  $(\Omega)$ , while  $j_0$  and  $\alpha$  are parameters that vary based on Z and A. ARTI integrates this flux equation over the chosen parameters to determine the number of particles of each type that will be injected into the simulation.

#### S1 Stage in ARTI: Secondary Particle Data Collection

Following the completion of the S0 stage, which generates a catalog of primary cosmic ray interactions, the S1 stage in ARTI focuses on extracting and organizing detailed information about the resulting secondary particles. This catalog produced in the S0 phase includes comprehensive data on the secondary particle flux, particle IDs, momenta, and positional information relative to the primary particles, along with details about each secondary particle's primary progenitor. This data serves as the foundation for the subsequent analysis and enables a deeper understanding of the secondary cosmic ray at ground level.

The S1 stage is primarily handled by the ARTI script do\_showers.sh. This script is responsible for collecting and organizing the information produced in the S0 stage into various output files, each containing specific details relevant to the analysis. The command to execute this script is as follows:

#### In this command:

- -o specifies the output directory where the resulting files will be saved, organized by the zenith angle range (\${theta}-\${thetamax}deg) and the simulation time.
- -k sets the altitude parameter for the simulations, configured here to 2200 meters above sea level (representing the altitude of Cumbayá).
- -t indicates the simulation time, ensuring that all collected data corresponds to the designated time period for each run.
- -1 is used to trigger the data collection mode for secondary particle information.

The output of the S1 stage includes several bzip2-compressed ASCII files, each containing specific data about the primary particles and the resulting secondaries. These files are essential for conducting detailed analyses of particle showers at ground level.

For this project, the .shw.bz2 file is particularly valuable, as it includes a comprehensive catalog of secondary particles at ground level along with relevant information about each particle's progenitor. This file enables a detailed analysis of the secondary particle flux and is essential for understanding the distribution and characteristics of secondary cosmic ray particles.

By automating the extraction and organization of this information, the S1 stage in ARTI significantly streamlines the workflow, allowing for efficient data handling and ensuring that the necessary data is readily available for further stages of analysis.

#### Automated Simulation Workflow with Integrated Run Script

To streamline the simulation process and automate parameter configuration, a custom script named integrated\_run.sh was developed. This script builds upon rungo.sh, which can be found in [11], and follows the organizational structure outlined in [12].

The integrated\_run.sh script relies on datos.txt as its input file, where key parameters for each simulation run are defined. These include **Time** (seconds), Height (meters), Distance in x (kilometers), Distance in y (kilometers), Zenith Angle (degrees), and Max Zenith Angle (degrees). For this study, the following configurations were applied:

- Time: Set to 600 seconds, representing the duration of each simulation in CORSIKA.
- **Height:** Corresponds to the altitudes at which secondary particles are simulated in CORSIKA and extracted for further propagation in Geant4.
- Zenith Angle and Max Zenith Angle: Define the angular range of primary particles entering the atmosphere, which for this project was set from 0 to 90 degrees, encompassing all possible cosmic ray trajectories.
- Distance in x: Set to zero.
- **Distance in y**: Corresponds to the fixed location of the region of interest: 5 km along the negative y-axis relative to the origin. This configuration aligns with the section 3.2, where the detector covers a 1 km × 1 km area at this specific position.

The script integrates with ARTI components (do\_sims.sh and do\_showers.sh) and the rungo.sh script to initiate and manage simulations. It automates the entire process, from preparing input parameters to managing execution and collecting results, thereby enhancing workflow efficiency.

Upon execution, integrated\_run.sh produces an output file named output.txt, which logs key parameters and results in a structured format. Each row in output.txt represents a single simulation and includes information on Simulation Time, Height, Distance in x, Distance in y, Zenith Angle (theta), Max Zenith Angle (theta\_max), Particles Detected, and Flux at Detector. Additionally, the script generates .shw.bz2 files for each simulation run. These files are critical to the workflow, containing detailed data on secondary particles simulated at 2200+H meters (the upper boundary of the Geant4 world). These particles are injected into the Geant4 simulation at the upper boundary and subsequently propagated through the simplified atmospheric model.

By centralizing input parameters in datos.txt and consolidating simulation outputs in output.txt, this script aligns the objectives of this project. All scripts and configurations are available in the associated GitHub repository for verification and further exploration [34].

### 3.4 Atmospheric model in Geant4

The atmospheric model plays a pivotal role in simulating the propagation of secondary particles, which are generated from the interaction of primary cosmic rays with the upper layers of the atmosphere. Using Geant4, this project models the propagation of these secondary particles, which are derived from CORSIKA simulations, through a simplified atmospheric representation. This approach enables the evaluation of secondary cosmic ray fluxes as they travel to lower altitudes, including ground level.

In particular, Geant4 integrates the secondary particles as inputs for the atmospheric model, creating a controlled environment to analyze how geo-electromagnetic field variations—potentially induced by seismic events—might alter the observed fluxes at ground level. This framework establishes a solid basis for exploring the potential influence of localized field anomalies, ensuring that both standard and anomalous conditions can be systematically studied within a unified simulation setup.

#### 3.4.1 Simulation Volume

The simulation volume in **Geant4** is designed to represent the atmospheric region where secondary cosmic ray particles propagate. Building on the framework established in the section 3.2, the simulation volume integrates the parameters **H**, **D**, **h**, **r**, and **d**, defining the dimensions and positioning of the modeled environment. These parameters ensure consistency between the representations in **Geant4** and the initial conditions derived from **CORSIKA** simulations.

#### **Volume Dimensions**

While the general configuration of the simulation volume has been established, specific details are fixed here to suit the computational requirements and capture the particle behavior effectively. The horizontal dimensions (**D**) span 2000 km in both width and length to fully encompass the expected dispersion of secondary particles. The vertical extent, **H**, is set to 100 m, ensuring a balance between computational efficiency and accuracy in simulating the propagation from the upper to the lower boundary.

To maintain physical relevance, the lower boundary represents an altitude of approximately 2200 m, corresponding to Cumbayá, Quito, and the upper boundary extends to  $2200 + \mathbf{H}$ . These dimensions provide a controlled environment for analyzing particle behavior while ensuring that secondary particles remain within the simulation world boundaries throughout their propagation.

#### Volume Geometry

The parallelepiped geometry of the Geant4 world remains consistent with the abstraction described earlier. This geometry, while simple, is effective in capturing the propagation of secondary particles from the upper boundary to the lower boundary without introducing computational overhead. The placement of the cylindrical Zone of Influence and the detector volume within this geometry allows for precise analysis of particle flux changes under varying conditions.

#### Subvolumes

Two distinct subvolumes are implemented within the Geant4 world volume, designed to facilitate the study of secondary particle fluxes and their interaction with geo-electromagnetic field variations:

#### 1. Detector Volume

The detector is modeled as a rectangular volume with dimensions of  $1 \text{ km} \times 1 \text{ km} \times 1 \text{ m}$ , located at the lower boundary of the simulation world, representing an altitude of 2200 m above sea level (Cumbayá, Quito). This detector is centered **5 km along** the negative y-axis, consistent with the region defined in CORSIKA for  $\Phi_t$ . The alignment ensures direct comparability between the fluxes  $\Phi_t$  and  $\Phi_g$ , as the detector volume measures  $\Phi_q$  within the same localized area.

#### 2. Zone of Influence (Affected Region)

The Zone of Influence is represented as a cylindrical volume with a **radius** (**r**) of 25 km and a height equal to **h**. This zone is used to model localized geo-electromagnetic field variations and can be repositioned within the simulation world to study how the horizontal distance **d** between the Zone of Influence and the fixed detector influences secondary particle flux measurements.

This design ensures flexibility to vary the position of the Zone of Influence while maintaining the detector fixed in its specified area, enabling a detailed and controlled analysis of the effects of **d** on secondary particle fluxes.

#### 3.4.2 Material Definition

The atmospheric medium in the simulation is represented by G4\_AIR, a predefined material in Geant4 specifically designed to model air properties. This material was chosen for its simplicity and accuracy in representing the general characteristics of the atmosphere. The properties of G4\_AIR include the following [7]:

- 1. **Density:**  $0.00120479 \text{ g/cm}^3$
- 2. Ionization Energy (I): 85.7 eV
- 3. Chemical Composition (fractional mass):
  - Nitrogen (N): 75.52676%
  - Oxygen (O): 23.17811%
  - Argon (Ar): 1.28273%
  - Carbon Dioxide ( $CO_2$ ): 0.01240%

#### **Model Simplification**

A homogeneous material was used to represent the atmosphere due to the relatively small height of the simulation volume ( $\mathbf{H}=100~\mathrm{m}$ ) in Geant4. At this scale, the atmosphere can be reasonably approximated as uniform. A more complex atmospheric profile, accounting for variations in density, temperature, and pressure with

altitude, would have been necessary for a larger model (e.g.,  $\mathbf{H} = 10 \text{ km}$ ). However, this was not feasible due to computational constraints, as simulations with a height of 10 km exceeded memory capacity and required prohibitively long runtimes.

Furthermore, the scope of this study focuses on the detection of secondary cosmic ray particles under local geo-electromagnetic field conditions. A homogeneous material model suffices for this purpose, as it allows for a straightforward assessment of whether local changes in geo-electromagnetic fields can influence the secondary cosmic ray flux detected at ground level. The simplified representation ensures computational efficiency without compromising the validity of the results for the intended research questions.

#### 3.4.3 Particle Injection

The injection of secondary particles into the Geant4 simulation is a critical process that bridges the outputs of CORSIKA with the atmospheric model in Geant4. These secondary particles, generated through detailed simulations in CORSIKA, are introduced at specific altitudes within the Geant4 environment to analyze their behavior under varying geo-electromagnetic field conditions. For this study, secondary particles are extracted from CORSIKA at an altitude corresponding to 2200 + H meters, aligning with the upper boundary of the Geant4 simulation world. This ensures consistency between the particle properties simulated in CORSIKA and their propagation through the atmospheric representation in Geant4. The process of generating secondary particles with CORSIKA can be found in Section 3.3.

#### **Injected Particle Properties**

The particles injected into the Geant4 simulation were characterized by the following properties, as determined by the CORSIKA output:

- Particle Type: A wide range of secondary particles, including muons, electrons, positrons, and hadrons.
- Energy: The energy spectrum of the particles as provided by CORSIKA.
- Momentum: Directional information, including the zenith and azimuthal angles.
- **Position:** The spatial distribution of particles at ground level, which serves as the input layer for Geant4.
- Primary Particle Information: Each secondary particle is accompanied by metadata identifying the primary particle from which it originated, enabling a more detailed understanding of the cascade process.

#### Injection Process in Geant4

To implement the injection of secondary particles into Geant4:

1. The output data from CORSIKA was converted into a format compatible with Geant 4.

- 2. A custom particle source was developed in Geant4 to read the CORSIKA output and initialize particles within the simulation volume.
- 3. Particles were injected at the upper boundary of the simulation world (**H** = 100 m) to simulate their continued propagation toward the ground-level detector.

Injecting secondary particles directly into the Geant4 simulation allows for a more focused study of the impact of local geo-electromagnetic field variations. Instead of modeling the entire atmospheric cascade, this approach targets the segment of the propagation most relevant to the ground-level particle flux under these conditions, optimizing computational resources while maintaining the accuracy of the results.

#### 3.4.4 Interaction Physics

The simulations in this study were conducted using version 10.7.3 of Geant4. This section focuses on the physical processes, numerical methods, and electromagnetic fields implemented in the simulation to analyze the propagation of secondary cosmic ray particles.

#### Physics List

In Geant4, a physics list defines the set of physical processes and models used to simulate the interactions of particles with matter. The physics list selected for this study is QGSP\_BERT, which is specifically designed to model both electromagnetic and hadronic interactions. This physics list is ideal for cosmic ray studies as it incorporates the physics of electromagnetic cascades and hadronic interactions over a wide range of energies, specifically from 0.1 GeV to 10 TeV [5]. For hadronic interactions, the physics list incorporates quark-gluon string (QGS) and Bertini cascade models, which accurately simulate inelastic collisions involving high-energy hadrons, such as protons and neutrons, with nuclei.

Although Geant4 does not directly implement the Matthews model for hadronic cascades [30], it provides advanced models, such as the quark-gluon string model, which captures the key physical processes described by the Matthews framework. These models include cross-section parameterizations for elastic and inelastic scattering, as well as decay processes for unstable particles. Together, these features allow Geant4 to simulate hadronic cascades effectively within the context of cosmic ray interactions.

#### **Electromagnetic Fields**

Electromagnetic fields were integrated into the simulation in two distinct configurations. First, a uniform geomagnetic field was applied across the entire simulation world to account for Earth's natural magnetic influence on particle trajectories. Second, a localized electric or magnetic field was implemented within the Zone of Influence, a cylindrical volume embedded in the simulation world. This volume was specifically designed to model the influence of seismic-induced geo-electromagnetic anomalies on secondary cosmic ray fluxes. The localized field setup utilized the

G4UniformElectricField class, with particle interactions managed through field managers and chord finders [6].

- **Field Managers:** These are responsible for managing the interactions between particles and the fields within specific regions of the simulation. They ensure that the correct field equations are applied in the designated volumes and control the integration of particle trajectories through these fields.
- Chord Finders: These tools approximate curved particle trajectories within fields by dividing them into smaller linear segments, or "chords." This approach allows Geant4 to efficiently determine where a particle intersects with volume boundaries or interacts with other regions in the simulation.

Numerical integration of particle trajectories through the electromagnetic fields was performed using the G4ClassicalRK4 method, a fourth-order Runge-Kutta algorithm. This method was selected for its accuracy and robustness in solving the equations of motion for charged particles in fields. A step size of 0.1 nm was used to balance computational efficiency with precision in trajectory calculations. The integration algorithm ensures that both electric and magnetic forces acting on particles, as well as the energy and curvature paths of particles under field influence, are accurately captured.

The Geant4 atmospheric model was validated against reference simulations from CORSIKA to ensure consistency in particle propagation. Initial runs without electric or magnetic fields were conducted to verify that secondary particle fluxes at ground level matched expected baseline values.

### 3.5 Containerization Workflow Using Docker

Docker is a platform designed to simplify the development, distribution, and execution of applications by packaging them into isolated environments called containers. These containers ensure that an application, along with all its dependencies and configurations, can run consistently across different systems. By providing a lightweight and efficient means to separate applications from their underlying infrastructure, Docker allows for seamless testing, sharing, and deployment. In this project, Docker is leveraged to containerize the simulation workflow, ensuring reproducibility and scalability [10]. Two distinct containers are utilized: one for the ARTI framework and CORSIKA simulations to extract secondary particle data, and another for running the Geant4 atmospheric model to analyze particle propagation under varying geo-electromagnetic conditions.

### 3.5.1 Docker Implementation in the Simulation Framework

To ensure portability, scalability, and efficient execution of the simulation framework across different computational environments, Docker was employed for containerizing the workflow. By encapsulating the required software, dependencies, and configurations within containers, Docker facilitates consistent performance across local and cloud-based infrastructures, such as Google Cloud Platform (GCP). The containerization process was divided into two distinct stages, each tailored to specific tasks within the simulation framework.

#### Stage 1: CORSIKA and Secondary Particle Data Extraction

The first container includes the complete ARTI framework, the CORSIKA simulation software, and additional tools such as custom Python scripts and the <code>integrated\_run.sh</code> script for automation. This container is responsible for simulating the interaction of primary cosmic rays with the atmosphere and extracting detailed information on the resulting secondary particles. Specifically, this stage generates secondary particle flux data at a selected altitude 2200+H, which serves as the input for subsequent simulations in <code>Geant4</code>.

The outputs of this stage, including .shw.bz2 files containing detailed secondary particle data, are stored in a shared location accessible to the second container.

#### Stage 2: Geant4 Atmospheric Model Simulation

The second container is built around the Geant4 simulation toolkit, with all necessary files and dependencies configured to simulate the propagation of secondary cosmic ray particles through the atmospheric model described in Section 3.4. The secondary particle data extracted in Stage 1, particularly the .shw.bz2 files, are transferred to this container to initialize the particle injection process in Geant4.

This stage executes the particle propagation model and computes the number of particles detected at ground level, corresponding to the detector volume within the Geant4 world. The results generated form the final dataset used for analyzing the influence of seismic-induced geo-electromagnetic field variations.

#### Advantages of Docker in the Workflow

Using Docker for containerization provides several key advantages:

- Reproducibility: The containerized environments ensure that the simulations can be consistently reproduced across different systems without discrepancies caused by software or configuration differences.
- **Portability:** Containers can be seamlessly deployed on local machines, HPC clusters, or cloud environments such as GCP.
- **Isolation:** Each stage of the workflow operates within its own container, preventing conflicts between software dependencies.
- **Automation:** The predefined Docker images and containerized scripts streamline the workflow, expediting setup time and minimizing human error.

By leveraging Docker, the simulation framework achieves a high degree of flexibility and efficiency, enabling complex workflows to be executed with ease and precision across varied computational environments. The Docker images used for this project can be found on DockerHub [25, 23], while the corresponding Dockerfile—used to build these images—is available on GitHub [24, 20]. These images were specifically designed to integrate seamlessly with the cloud computing workflows detailed in Section 3.6, where YAML files are utilized to pull the ready-to-use images from DockerHub and deploy them as containers in a scalable cloud environment.

# 3.6 Computational Resources and Environment Setup

#### 3.6.1 Parallelization and Scalability

The computational intensity of the simulations required the use of parallel processing to reduce runtime. To manage this, Google Kubernetes Engine (GKE) on Google Cloud Platform (GCP) was utilized, offering a flexible and scalable environment for containerized simulations. GKE enabled the automatic deployment, scaling, and management of containers across a multi-node cluster, which streamlined the process of running numerous simulations in parallel [14].

The setup began by configuring a new GCP project and enabling the Kubernetes API, allowing GKE to orchestrate and manage the cluster. The Kubernetes cluster was created with the following specifications:

• Zone: us-central1-a

• Number of Nodes: 5

• Machine Type: e2-standard-4

• Total Memory: 80 GB

• Total vCPUs: 20

The cluster was configured in the us-central1-a zone, providing a reliable environment with low latency for accessing cloud resources. While each simulation runs independently without the need for node-to-node communication, low latency helps ensure quick access to storage and cloud services, which supports efficient data handling and resource allocation during intensive simulation tasks.

Each of the 5 nodes used the e2-standard-4 machine type, equipped with 4 virtual CPUs (vCPUs) and 16 GB of RAM per node, delivering adequate resources for running high-performance simulations efficiently. This setup offered a total of 20 vCPUs and 80 GB of memory across the cluster, enabling it to handle multiple parallel jobs effectively.

After the cluster setup, kubectl was configured to interact with the cluster, facilitating efficient management and monitoring of job distribution across the nodes. The use of GKE enabled automatic scaling and workload balancing, ensuring the cluster's computational resources were utilized effectively. YAML configuration files were essential for this process, specifying essential parameters such as the Docker image to be pulled from DockerHub, resource limits, environment variables, and the number of parallel jobs. These configurations ensured that the containers created from the Docker images were fully prepared to execute the simulations, encapsulating all necessary software and dependencies to guarantee consistency, reproducibility, and seamless deployment across the computational environment.

### 3.6.2 Data Storage and Management

To handle the extensive data generated by the simulations, a Google Cloud Storage (GCS) bucket was created. This bucket served as the central repository for storing

intermediate and final results from each simulation run. Ensuring secure access to GCS was a priority, especially as data needed to be transferred from multiple containers simultaneously.

Data security and access management were handled using a service account on GCP, which was assigned specific permissions to access the GCS bucket. This service account's credentials were mounted as a secret within each Kubernetes pod, enabling authenticated access to the storage bucket without exposing sensitive information. Each containerized simulation could then upload its results directly to the GCS bucket, ensuring both data security and efficient data handling.

#### 3.6.3 Cost Optimization

To optimize resource usage and control costs, GCP's pricing options were carefully leveraged, including the use of preemptible instances. These cost-effective instances were selected for non-critical or repeatable tasks, as they can be interrupted by Google Cloud if resources are needed elsewhere. This strategic choice helped reduce costs without compromising essential workloads. Additionally, the project utilized the \$300 in free credits provided by GCP, allowing for efficient resource allocation within the budget.

Auto-scaling was also enabled within the Kubernetes cluster, allowing GKE to automatically adjust the number of nodes based on workload demand. This feature dynamically increases resources during high-demand periods, ensuring sufficient capacity for running multiple simulations, and reduces resources during lower-demand periods by scaling down unused nodes. By allocating resources only as needed, auto-scaling optimized resource usage and helped further reduce unnecessary costs.

## 3.7 Uncertainty Analysis

The uncertainty analysis is essential to evaluate the reliability of the results obtained in this study, as both CORSIKA and Geant4 rely on Monte Carlo algorithms, which inherently introduce statistical fluctuations. Additionally, the design and configuration of the simulation framework may introduce systematic uncertainties that must also be considered.

#### 3.7.1 Statistical Uncertainties

Statistical uncertainties arise from the stochastic nature of Monte Carlo algorithms used in CORSIKA and Geant4. These uncertainties are estimated by running multiple independent simulations, allowing the calculation of:

- Mean ( $\Phi_{\text{mean}}$ ): Represents the average value of secondary fluxes obtained from N independent simulations.
- Standard deviation ( $\sigma_{\text{statistical}}$ ): Represents the spread of the results across simulations due to the random nature of the computations.
- Coefficient of Variation (CV): Represents the relative variability of the secondary fluxes by normalizing the standard deviation ( $\sigma_{\Phi}$ ) to the mean ( $\Phi_{\text{mean}}$ ).

It is expressed as a percentage:

$$CV = \frac{\sigma_{\Phi}}{\Phi_{\text{mean}}} \times 100. \tag{3.2}$$

• Relative Uncertainty ( $\epsilon_{rel}$ ): The relative uncertainty between the means of  $\Phi_t$  (from CORSIKA) and  $\Phi_q$  (from Geant4) is calculated as:

$$\epsilon_{\rm rel}(\%) = \frac{|\Phi_t - \Phi_g|}{\Phi_t} \times 100 \tag{3.3}$$

This formula quantifies the percentage difference between the two fluxes, allowing for a direct comparison of their agreement.

For this study, the statistical uncertainties are evaluated as follows:

• For  $\Phi_t$ , obtained from CORSIKA, 20 independent simulations are conducted using the following parameters:

- Time: 600 seconds.

- **Height:** 2300 m.

- Zenith Angle:  $0-90^{\circ}$ .

- Distance in x: 0 km.

- Distance in y: -5 km.

• For  $\Phi_g$ , obtained from Geant4, 20 independent simulations are also conducted without any electric or magnetic fields in the Zone of Influence, using the .shw.bz2 file generated by CORSIKA as input (details in section 3.4).

The total statistical uncertainty is propagated considering that Geant4 uses input from CORSIKA. The total uncertainty is calculated as:

$$\Delta \Phi = \sqrt{\sigma_{\text{CORSIKA}}^2 + \sigma_{\text{Geant4}}^2} \tag{3.4}$$

where  $\sigma_{\text{CORSIKA}}$  and  $\sigma_{\text{Geant4}}$  represent the independent statistical uncertainties from CORSIKA and Geant4, respectively. This ensures that the final result for  $\Phi_g$  includes the statistical contributions from both simulations.

#### Systematic Uncertainties

Systematic uncertainties reflect potential biases introduced by methodological decisions and specific simulation configurations. These may arise from:

- Geometric configuration: Simplifications in the atmospheric model used in Geant4, such as the assumption of a homogeneous atmosphere instead of a more realistic atmospheric profile.
- Physics models: The selection of a single hadronic interaction model (QGSJET-II04) and electromagnetic interaction model (EGS4) in CORSIKA.

• Random seeds: In CORSIKA, the seeds are automatically assigned by the do\_sims.sh script, ensuring randomization between simulations. In contrast, in Geant4, a fixed seed is used, which could limit the exploration of variability inherent to the model.

For this analysis, systematic uncertainties were not directly quantified due to the absence of specific sensitivity studies or comparative analyses.

Since no quantitative estimate for sistematic uncertainties is available in this study, systematic uncertainties are excluded from the total uncertainty calculation. The final result is reported as:

$$\Phi_g \pm \Delta \Phi \tag{3.5}$$

where  $\Delta\Phi$  is dominated by statistical uncertainties.

## Chapter 4

## Results and Discussions

This chapter presents the results and analysis derived from the simulations conducted to evaluate the impact of seismic-induced geo-electromagnetic field variations on secondary cosmic ray fluxes. Section 4.1 focuses on validating the simulation framework, comparing the fluxes obtained from CORSIKA and Geant4 under baseline conditions, and addressing the observed discrepancies between the two frameworks. Section 4.2 quantifies the uncertainties inherent in the simulation results, establishing confidence ranges and variability metrics critical for identifying significant deviations attributable to geo-electromagnetic influences. Section 4.3 examines the implementation and effects of geo-electromagnetic fields within the Geant4 framework, analyzing whether these variations induce detectable changes in secondary cosmic ray flux at ground level. Finally, Section 4.4 discusses the computational challenges encountered during the simulation process, detailing the optimizations made to overcome resource limitations and ensure the successful execution of large-scale simulations.

#### 4.1 Validation of the Simulation Framework

The validation of the simulation framework is a critical step to ensure the consistency and reliability of the tools and methodologies employed in this study. This section focuses on comparing the secondary particle flux  $\Phi_t$ , obtained from CORSIKA simulations, with the corresponding flux  $\Phi_g$ , derived from Geant4 under similar conditions. While the two frameworks share comparable input configurations, differences in atmospheric modeling, particle interaction physics, and simulation methodologies may contribute to discrepancies in the results. This comparison not only establishes the reliability of Geant4 in propagating secondary particles but also validates the framework as a whole, providing confidence for further analyses.

Table 4.1 summarizes the results of 20 independent simulations performed with CORSIKA. To calculate the flux  $(\Phi_t)$  in particles/m<sup>2</sup>s, the total number of secondary particles recorded during each simulation was divided by the simulated detector area  $(1 \text{ km}^2)$  and the simulation time (600 s). The resulting flux values were then normalized to the muon flux observed in a Cherenkov detector located in Quito, as referenced in [35], to provide a standardized comparison. From these simulations, the following statistical results were obtained:

• The mean value of the secondary particle flux:

$$\Phi_t = 150 \, \frac{\text{particles}}{\text{m}^2 \, \text{s}}.\tag{4.1}$$

• The standard deviation of  $\Phi_t$  across the simulations:

$$\sigma_{\Phi_t} = 5 \frac{\text{particles}}{\text{m}^2 \,\text{s}}.\tag{4.2}$$

• The coefficient of variation (CV) is given by:

$$CV = \frac{\sigma_{\Phi_t}}{\Phi_t} \times 100 = \frac{5}{150} \times 100 = 3.33\%.$$
 (4.3)

Consequently, the final result for the flux is expressed as:

$$\Phi_t = 150 \pm 5 \frac{\text{particles}}{\text{m}^2 \text{ s}}.$$
(4.4)

These results provide a robust statistical baseline for validating the secondary particle flux simulated using CORSIKA, establishing a reference point for comparisons with the Geant4 simulations.

Simulation	$\Phi_t$ (particles/m <sup>2</sup> s)		
1	146		
2	147		
3	145		
4	141		
5	143		
6	154		
7	148		
8	152		
9	151		
10	156		
11	154		
12	148		
13	143		
14	151		
15	156		
16	154		
17	148		
18	152		
19	151		
20	156		

Table 4.1: Results of 20 independent CORSIKA simulations, showing the calculated secondary particle flux  $(\Phi_t)$  in particles/m<sup>2</sup>s.

For the Geant4 simulations, the detector configuration is defined as a subvolume within the simulation world, positioned at a fixed distance of -5 km along the y-axis

relative to the origin. The detector spans a square area of  $1 \,\mathrm{km} \times 1 \,\mathrm{km}$  at ground level, corresponding to an altitude of 2200 m above sea level, as described in 3.4.1.

During this phase of validation, the Zone of Influence, modeled as a cylindrical volume within the Geant4 world, does not include any electric or magnetic fields. This configuration ensures that the simulations reflect baseline conditions, focusing solely on the secondary particle flux  $\Phi_g$  detected at ground level.

The comparison of  $\Phi_g$  with  $\Phi_t$ , obtained from CORSIKA, provides a preliminary validation of the consistency between the two simulation frameworks under standard conditions.

Using 20 independent simulations, the average flux at the detector was computed, along with the associated standard deviation and uncertainty. The final result for the flux  $\Phi_q$ , under these conditions, is expressed as:

$$\Phi_g = 188 \pm 2 \,\text{particles/m}^2 \text{s.} \tag{4.5}$$

The coefficient of variation (CV) of  $\Phi_q$  is:

$$CV = 1.15\%.$$
 (4.6)

The relative uncertainty between the fluxes obtained from CORSIKA and Geant4 simulations was calculated using the equation 3.3.

Substituting the values,  $\Phi_t = 150 \, \text{particles/m}^2 \text{s}$  and  $\Phi_g = 188 \, \text{particles/m}^2 \text{s}$ , the relative uncertainty is:

$$\epsilon_{\rm rel}(\%) = \frac{|150 - 188|}{150} \times 100 \approx 25.3\%$$
(4.7)

This result indicates a relative discrepancy of approximately 25.3% between the two simulation frameworks. This significant difference underscores the importance of examining the modeling assumptions and implementations in CORSIKA and Geant4, as discussed below.

The observed discrepancy between  $\Phi_t = 150 \pm 5$  particles/m<sup>2</sup>s (from CORSIKA) and  $\Phi_g = 188 \pm 2$  particles/m<sup>2</sup>s (from Geant4) can be attributed to several factors related to the modeling approaches and assumptions in each simulation framework.

Firstly, the simplified atmospheric model used in Geant4 could significantly contribute to the differences. Unlike CORSIKA, which simulates particle propagation using a layered atmospheric profile with varying density, temperature, and pressure, Geant4 employs a homogeneous atmospheric medium (G4\_Air) without such variations (details in Section 3.4.2). Although this simplification is reasonable within the 100 m height of the Geant4 world, it does not account for the specific atmospheric conditions at an altitude of 2200–2300 m, such as density, temperature, and pressure. These factors could significantly affect the particle flux, especially for high-energy particles sensitive to small variations in atmospheric conditions [36]. As a result, the homogeneous approximation may oversimplify key processes, potentially leading to discrepancies in the flux observed at ground level. Furthermore, alternative configurations, such as employing sequences of smaller world volumes or refining the geometry to better represent realistic atmospheric layers, could improve the agreement with CORSIKA.

Additionally, the number of simulations performed and the seed configurations used in both frameworks may also play a role. In CORSIKA, the seeds for the Monte

Carlo algorithm are varied automatically for each simulation, ensuring statistical independence. Conversely, Geant4 simulations used a fixed seed configuration, which could slightly constrain the variability in the resulting fluxes. While this difference may seem minor, it highlights how specific simulation setups can impact the final results.

Lastly, while the number of simulations performed (20 in CORSIKA and 20 in Geant4) is sufficient for statistical analysis, increasing the sample size could further reduce statistical uncertainties and improve the robustness of the comparison. A larger number of runs would allow for better characterization of the variability within each framework, offering a more precise understanding of the observed discrepancies.

It is important to emphasize that the primary objective of this study is to validate the methodological approach and exercise the infrastructure developed for these simulations. Refinements, such as incorporating layered atmospheric profiles or exploring alternative geometric configurations in Geant4, represent future improvements that can be pursued as part of the continuous development of these tools. By addressing these limitations, the framework can achieve greater consistency and reliability in simulating cosmic ray interactions with the Earth's atmosphere.

## 4.2 Uncertainty Quantification for Geo-Electromagnetic Influences

The analysis of the impact of geo-electromagnetic variations on secondary cosmic ray flux requires considering the combined uncertainties from both simulation frameworks. The flux  $\Phi_g$  from Geant4 incorporates secondary particles propagated under specific atmospheric conditions, with these particles originating from the CORSIKA flux  $\Phi_t$ . Each of these fluxes has an associated uncertainty:  $\sigma_{\text{CORSIKA}} = 5 \, \text{particles/m}^2 \, \text{s}$  for CORSIKA, and  $\sigma_{\text{Geant4}} = 2 \, \text{particles/m}^2 \, \text{s}$  for Geant4.

The flux measured in the Geant4 simulations is  $\Phi_g = 188 \pm 2 \,\mathrm{particles/m^2}\,\mathrm{s}$ . This value represents the mean flux of secondary cosmic rays detected under conditions with no geo-electromagnetic perturbations, with the uncertainty reflecting only the variability inherent to the Geant4 simulations. Specifically, these unperturbed conditions indicate the absence of any applied electric or magnetic fields in the Zone of Influence within the Geant4 model.

To account for the combined uncertainties, the total uncertainty  $\Delta\Phi$  is calculated using equation 3.4:

$$\Delta \Phi = 5 \, \text{particles/m}^2 \text{s} \tag{4.8}$$

Under these conditions, the baseline flux with the total uncertainty, which includes contributions from the uncertainties in both simulation frameworks, is reported as:

$$\Phi_g = 188 \pm 5 \,\text{particles/m}^2 \text{s} \tag{4.9}$$

The inclusion of the total uncertainty ensures that the reported flux accounts for the variability introduced by the CORSIKA input flux as well as the Geant4 propagation model, providing a more comprehensive measure of the flux under unperturbed conditions. This distinction is critical for accurately interpreting the baseline flux and identifying deviations attributable to potential geo-electromagnetic influences. The combined uncertainty and statistical variability of the secondary particle flux allow us to establish a confidence range and evaluate whether observed flux variations are due to electromagnetic influences or inherent simulation noise.

#### Confidence Range

The acceptable range of values (without considering anomalies) is defined by the following expression:

$$\Phi_g - \Delta \Phi \le \Phi_g \le \Phi_g + \Delta \Phi. \tag{4.10}$$

For the obtained results, this corresponds to:

$$183 \le \Phi_g \le 193. \tag{4.11}$$

#### Coefficient of Variation

Additionally, the coefficient of variation (CV) is calculated to provide a relative measure of the total uncertainty normalized with respect to the mean flux:

$$CV = \frac{\Delta\Phi}{\Phi_q} \times 100 = \frac{5}{188} \times 100 = 2.66\%.$$
 (4.12)

This indicates that the combined uncertainty represents 2.66% of the mean flux detected under unperturbed conditions.

#### Interpretation of Results

- Within the range: Any measurement of  $\Phi_g$  falling within the interval [183, 193] is considered consistent with simulations under unperturbed conditions. Variations in this range are attributable solely to inherent uncertainties in the simulations.
- Outside the range: If  $\Phi_g$  values exceed this range (e.g., > 183 or < 193), they are likely caused by significant influences of electromagnetic fields in the impact zone. Such values indicate anomalies that go beyond the variability explained by statistical uncertainty and inherent noise.

The confidence range and coefficient of variation are critical tools to discern whether observed flux changes are due to statistical noise or the physical effects of applied electromagnetic fields. Measurements within the range suggest that particle interactions perturbations caused by the applied fields, whereas values outside the range reflect only the baseline variability of the simulation framework. This ensures a robust methodology for identifying meaningful deviations in the context of geo-electromagnetic influences.

### 4.3 Impact of Geo-electromagnetic Variations

## 4.3.1 Validation of Geo-Electromagnetic Field Implementation

To ensure the proper implementation and functionality of the applied geo-electromagnetic fields in the Geant4 simulations, a validation test was conducted using a simplified

setup. This test involved creating a dedicated Geant4 world, within which a cylindrical region was defined. While the specific electric or magnetic field configurations differed from those used in the main study, the method of implementing the fields in this validation was identical to the approach applied throughout the development of this project. This ensured that the implementation technique was robust and consistent across all simulations.

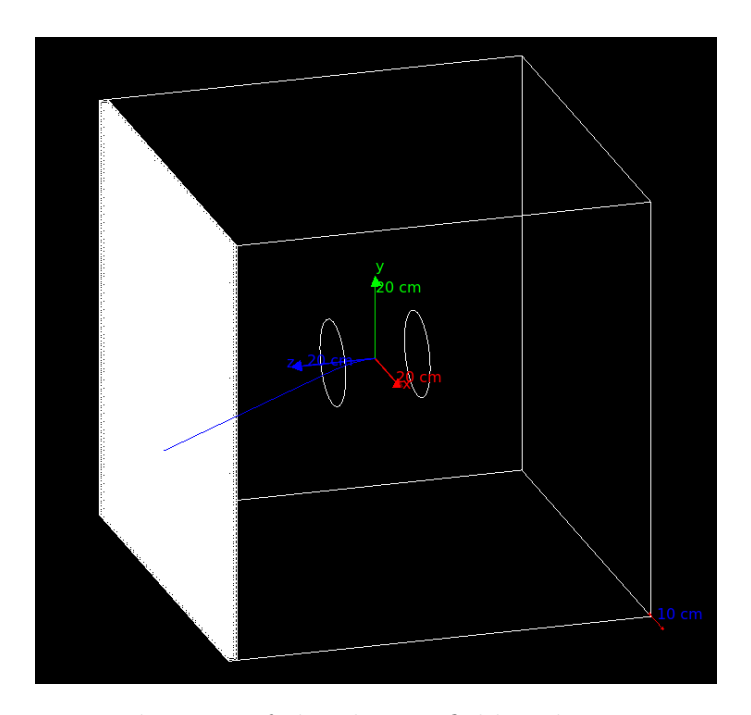


Figure 4.1: Visualization of the electric field and geometry in Geant 4.

For the validation, a single proton was introduced into the Geant4 world. The proton was assigned an energy of 0.01 GeV, representative of secondary particles observed in cosmic ray cascades. The proton was set to travel in a straight line along the z-axis of the simulation world.

Within the cylindrical region, an electric field of  $400,000\,\mathrm{V/m}$  was applied, oriented along the negative y-axis. This field configuration was chosen to exert a perpendicular force on the proton, as dictated by the Lorentz force law. Upon entering the cylindrical region, the proton's trajectory deviated as expected, confirming the field's proper implementation.

Figure 4.1 illustrates the proton's trajectory: it initially follows a straight path through the field-free region. Upon entering the cylindrical region containing the applied electric field, its trajectory deviates, consistent with the expected behavior of a charged particle under such conditions. The direction and magnitude of the deviation align with the parameters of the applied field.

This validation confirms that the geo-electromagnetic field implementation in Geant4 operates as intended. By demonstrating the correct behavior in this controlled environment, confidence is established in the methodology used to apply fields in the primary study. Ensuring that the implementation is consistent and functional is critical for accurately studying the effects of these fields on secondary cosmic ray fluxes.

# 4.3.2 Analysis of Geo-Electromagnetic Field Effects on Secondary Cosmic Ray Flux

The results presented in Table 4.2 demonstrate the impact of geo-electromagnetic variations on the secondary cosmic ray flux  $\Phi_g$  detected at the ground-level detector. The simulations were conducted under varying configurations of magnetic field strength (B) and electric field strength (E), with the Zone of Influence defined by a fixed height  $(\mathbf{h}=100\,\mathrm{m})$  and radius  $(\mathbf{r}=25\,\mathrm{km})$ . All measured flux values in Table 4.2 fall within the defined confidence range of [183, 193] particles/m<sup>2</sup>s. This indicates that none of the simulations exhibit deviations beyond the combined uncertainty  $\Delta\Phi=5\,\mathrm{particles/m^2}$ , suggesting that the observed fluctuations in flux values are consistent with statistical variations. Additionally, the coefficient of variation CV=2.66% confirms that the variability in  $\Phi_g$  across the different configurations remains within acceptable statistical limits. This supports the conclusion that the fluctuations in flux values are a result of inherent simulation uncertainties rather than external influences.

To visualize the impact of varying magnetic and electric fields on the secondary cosmic ray flux, Figures 4.2 and 4.3 present the flux as a function of distance for different field strengths. Figure 4.2 illustrates the flux variations with magnetic field strengths of  $2.84 \times 10^{-5}$  T,  $1 \times 10^{-7}$  T,  $1 \times 10^{-5}$  T, and  $1 \times 10^{-3}$  T. Figure 4.3 shows the flux variations for electric fields of 20, 50, and 100 V/m. In both figures, the uncertainty in the flux is represented by error bars.

The introduction of magnetic fields (B) ranging from  $1 \times 10^{-7}$ , T to  $1 \times 10^{-3}$ , T, and electric fields (E) ranging from 20, V/m to 100, V/m, does not produce any measurable deviations in the flux outside the confidence range. To further test the impact of stronger fields, an additional simulation (Simulation 31 in Table 4.2) was performed at a distance of 30 km from the detector with an electric field strength of  $3 \times 10^6$ , V/m. This field strength is comparable to the dielectric breakdown strength of air, which is sufficient to induce observable electromagnetic phenomena. However, even under these extreme conditions, the measured flux  $\Phi_g$  remained within the established confidence range, indicating no significant deviation from the baseline values.

This result highlights that even with exceptionally strong electric fields, the influence on the secondary cosmic ray flux is minimal. One possible explanation for this observation is that the particles traversing the Zone of Influence at 30 km originate primarily from lateral showers, which contribute less significantly to the total flux at the detector. The effects of the applied fields on these lateral particles are diluted by the overwhelming contribution of central showers, which dominate the particle flux and are less affected by localized electromagnetic perturbations. Furthermore, the energy and momentum characteristics of the secondary particles may render them resistant to deflection under the tested field strengths, further minimizing any measurable impact.

Overall, these findings suggest that the applied field configurations, even when scaled to extreme values, are insufficient to induce noticeable perturbations in the secondary cosmic ray flux at the ground-level detector. This underscores the robustness of the flux measurements and indicates that any future studies aiming to observe geo-electromagnetic effects will require either significantly larger field strengths or a more targeted approach to analyze the specific components of the secondary flux

#	d (km)	B (T)	E (V/m)	$\phi_g$ (particles/m <sup>2</sup> s)
1	30	$2.84 \times 10^{-5}$	-	185
2	30	$1 \times 10^{-7}$	-	189
3	30	$1 \times 10^{-5}$	-	186
4	30	$1 \times 10^{-3}$	-	188
5	30	-	20	188
6	30	-	50	187
7	30	-	100	188
8	90	$2.84 \times 10^{-5}$	-	189
9	90	$1 \times 10^{-7}$	-	190
10	90	$1 \times 10^{-5}$	-	187
11	90	$1 \times 10^{-3}$	-	187
12	90	-	20	186
13	90	-	50	188
14	90	-	100	189
15	150	$2.84 \times 10^{-5}$	-	190
16	150	$1 \times 10^{-7}$	-	185
17	150	$1 \times 10^{-5}$	-	185
18	150	$1 \times 10^{-3}$	-	191
19	150	-	20	186
20	150	-	50	189
21	150	-	100	192
22	250	$1 \times 10^{-5}$	-	191
23	250	$1 \times 10^{-3}$	-	188
24	250	-	20	190
25	250	-	50	190
26	250	-	100	187
27	300	$1 \times 10^{-5}$	_	187
28	300	$1 \times 10^{-3}$	-	190
29	300	-	50	187
30	300	-	100	185
31	30	-	$3 \times 10^{6}$	189

Table 4.2: Simulation parameters: distance (d), magnetic field (B), electric field (E), and particle flux  $\phi_g$  in particles/m<sup>2</sup> s.

most susceptible to such influences.

# 4.4 Simulation Framework Computational Challenges and Solutions

The execution of simulations on the Google Cloud Platform (GCP) presented significant computational challenges, necessitating careful optimization of simulation parameters to ensure successful completion. As detailed in Section 3.6, the simulations utilized Kubernetes clusters managed via Google Kubernetes Engine (GKE). Two free-tier GCP accounts, each with a budget of \$300, were employed, with identical cluster configurations across both accounts. Each cluster consisted of five nodes

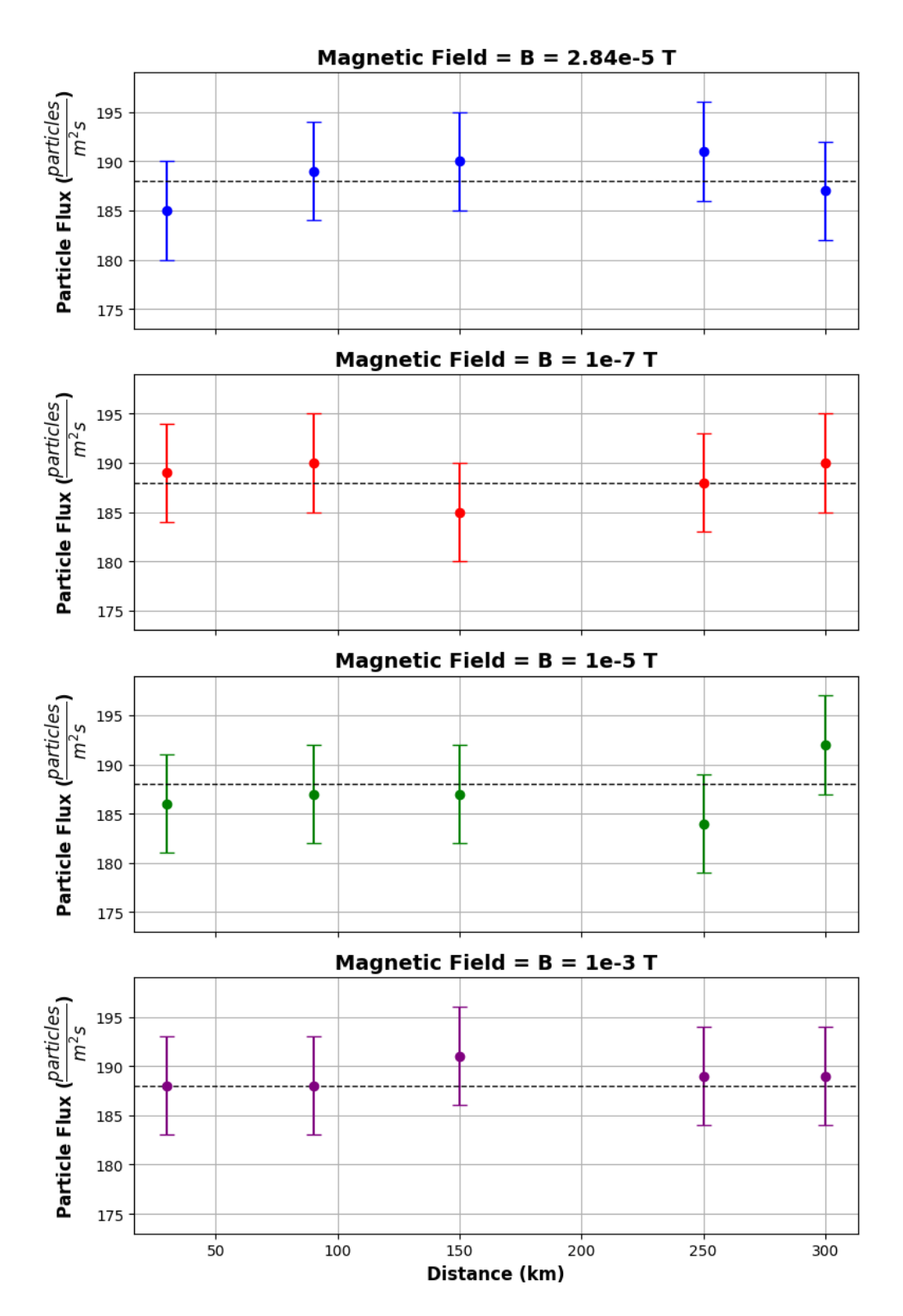


Figure 4.2: Particle flux as a function of distance for different magnetic field strengths (2.84e-5 T, 1e-7 T, 1e-5 T, 1e-3 T). The uncertainty in the flux is represented by error bars.".

of type c2-standard-4, providing a total of 20 vCPUs and 80 GB of memory per cluster, allowing for a maximum of 10 nodes across the two accounts. This setup enabled parallel processing, with one simulation running per node.

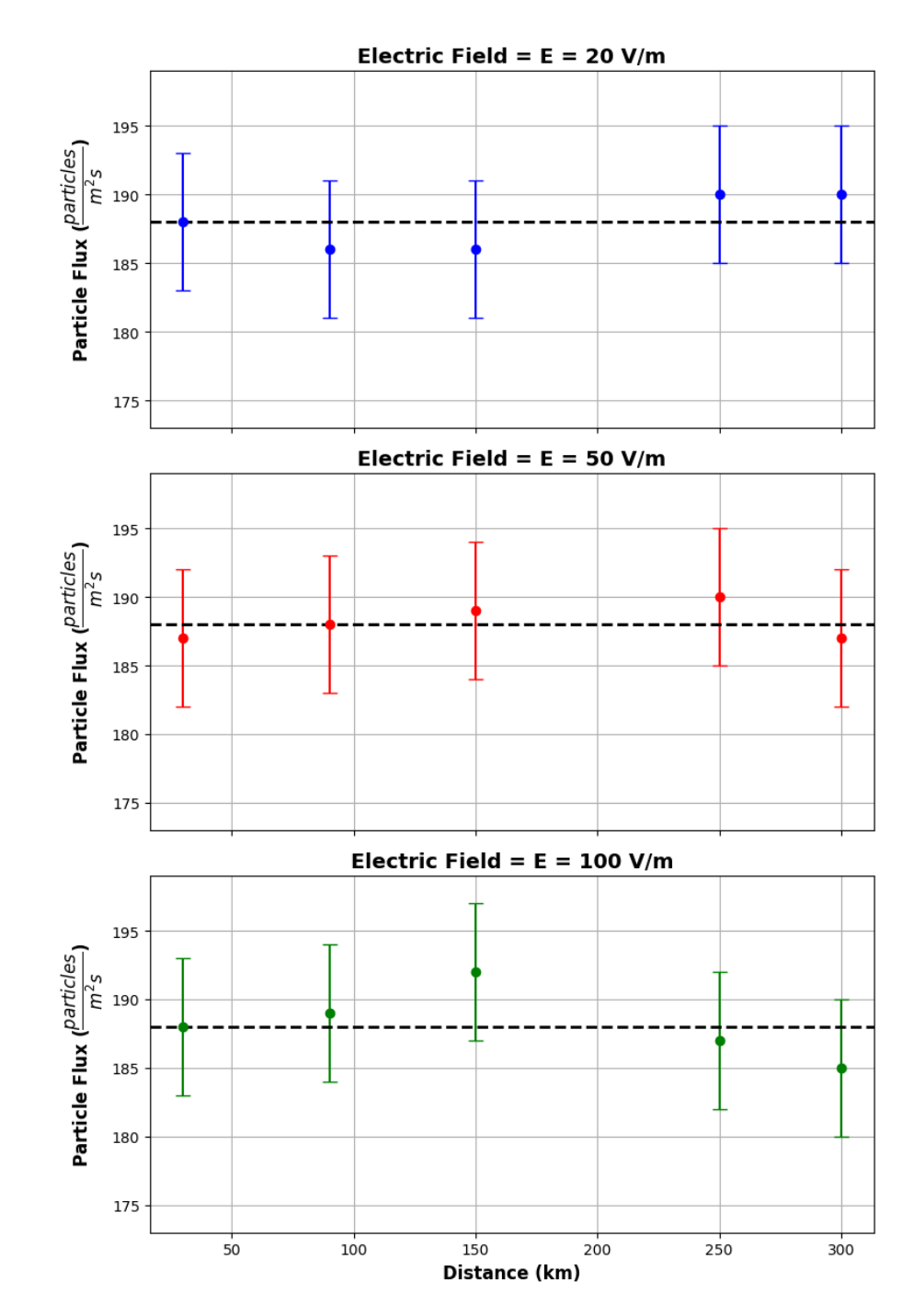


Figure 4.3: Particle flux as a function of distance for different electric field strengths (20, 50, and 100 V/m). The uncertainty in the flux is represented by error bars.

The simulation configurations were managed using YAML files, which defined parameters such as completions (total number of simulation runs) and parallelism (number of simulations executed concurrently). Resource limits were also specified, capping memory usage at 16 GB and CPU usage at 4 vCPUs per simulation. These configurations ensured optimal utilization of the available cloud resources while preventing system overload.

For CORSIKA, the runtime was dictated by the -t parameter in the do\_showers.sh script 3.3.2, which specified the duration of the simulated showers. Simulations set to a runtime of 2000 seconds required approximately 3 hours to complete and pro-

duced around 5 million secondary particles at the target altitude. However, these longer simulations frequently failed due to the resource limitations of the cluster. To mitigate this, the runtime was reduced to 600 seconds, reducing the simulation time to approximately 1 hour. This adjustment significantly improved the success rate, allowing for a greater number of simulations to be conducted within the cloud's resource constraints.

Similarly, Geant4 simulations initially utilized a world volume height of 10 km to capture a substantial portion of the atmosphere. However, this configuration required an average of 54 hours per simulation, often exceeding the memory and processing capabilities of the cluster, particularly when electromagnetic fields were applied. Attempts to reduce the world height to 1 km improved the runtime to 10 hours but still resulted in a high failure rate. These failures were attributed to the hardware limitations of the cluster, as each node was limited to 16 GB of RAM and 4 virtual CPUs. Furthermore, increasing the completion or parallelism values in the YAML files only exacerbated the failure rates, making large-scale parallel processing infeasible.

To address these issues, the world volume height in Geant4 was reduced to 100 m, cutting the simulation time to approximately 40 minutes to 1 hour per run. This adjustment struck a balance between computational feasibility and the ability to perform a sufficient number of simulations for comprehensive analysis. Combined with the reduced runtime in CORSIKA, these optimizations ensured the successful completion of all required simulations while maintaining the reliability of the results.

These resource-driven adjustments highlight the importance of tailoring simulation configurations to the computational infrastructure. The experience underscores the necessity of balancing computational demands with available resources, particularly when working within the constraints of cloud-based environments. By refining parameters such as runtime and world volume dimensions, the study was able to overcome the computational challenges posed by both simulation frameworks, ensuring robust and reliable outcomes.

## Chapter 5

## Conclusions

This study investigated the potential impact of seismic-induced geo-electromagnetic field variations on secondary cosmic ray fluxes, using advanced simulation tools to determine whether such effects are detectable at ground-level detectors. The study integrated CORSIKA to simulate the extensive air showers (EAS) produced by the interactions of primary cosmic rays with the atmosphere, and Geant4 for modeling the propagation of the secondary cosmic rays generated in these showers, including their interaction with seismic-induced geo-electromagnetic fields. By examining various configurations of electric and magnetic fields and analyzing the resulting secondary cosmic ray fluxes, this work contributes to the broader understanding of the potential influence of localized seismic-induced geo-electromagnetic disturbances on particle detection.

The results from CORSIKA and Geant4 simulations revealed a relative discrepancy of 25.3% between the two simulation frameworks, specifically when Geant4 simulations were conducted without the influence of any electric or magnetic fields. This discrepancy highlights the need for further scrutiny of the assumptions and implementations within each model, particularly regarding atmospheric conditions, field configurations, and simulation parameters. Such differences suggest that both frameworks require further refinement to ensure more consistent results, especially in the context of modeling high-energy particle interactions.

Simulations with varying magnetic and electric field strengths did not result in measurable deviations in the secondary cosmic ray flux  $(\Phi_g)$  outside the confidence interval of [183, 193] particles/m<sup>2</sup> s. Even when extreme electric fields of  $3 \times 10^6$  V/m were applied, no significant perturbations in the flux were observed. These results suggest that, under the conditions tested, seismic-induced geo-electromagnetic variations are not sufficiently strong to induce noticeable deviations in the secondary cosmic ray flux at ground level.

Computational challenges arose during the execution of the simulations on cloud platforms such as Google Cloud Platform (GCP). These challenges required optimizing simulation parameters, including reducing the atmospheric volume size in Geant4 and adjusting the simulation duration in CORSIKA. These adjustments were critical to ensuring the successful completion of simulations without exceeding available computational resources, while maintaining result reliability. The use of GCP enabled parallelization, allowing multiple simulations to run simultaneously, which greatly improved the efficiency of the computational process. However, resource limitations and hardware constraints, such as memory and CPU capacity, required

the optimization of simulation runtimes.

The findings of this study suggest that seismic-induced geo-electromagnetic variations, under the conditions tested, do not produce detectable deviations in the secondary cosmic ray flux at ground level. However, this study serves as a first step in exploring the interaction between seismic-induced geo-electromagnetic variations and cosmic ray propagation, laying the groundwork for future advancements in the detection and analysis of such effects. Future work could focus on refining simulation models and incorporating more realistic atmospheric conditions to better understand the potential impact of geo-electromagnetic disturbances on secondary cosmic ray fluxes.

## Bibliography

- [1] Sea Agostinelli et al. "GEANT4—a simulation toolkit". In: Nuclear instruments and methods in physics research section A: Accelerators, Spectrometers, Detectors and Associated Equipment 506.3 (2003), pp. 250–303.
- [2] HERNAN ASOREY. "Measurement of low energy cosmic radiation with the water Cherenkov detector array of the Pierre Auger observatory". In: *The Pierre Auger Observatory III: Other Astrophysi-cal Observations* (2011), p. 41.
- [3] Hernán G Asorey. "Los detectores Cherenkov del observatorio Pierre Auger y su aplicación al estudio de fondos de radiación". PhD thesis. Universidad Nacional de Cuyo, 2012.
- [4] Giuseppe Cocconi. "Influence of the Earth's Magnetic Field on the Extensive Air Showers". In: *Physical Review* 93.3 (1954), p. 646.
- [5] Geant4 Collaboration. Geant4 Physics List Guide. Accessed: November 21, 2024. 2024. URL: https://geant4-userdoc.web.cern.ch/UsersGuides/PhysicsListGuide/fo/PhysicsListGuide.pdf.
- [6] Geant4 Collaboration. Geant4 User's Guide for Application Developers. Accessed: November 21, 2024. URL: https://geant4-userdoc.web.cern.ch/UsersGuides/ForApplicationDeveloper/fo/BookForApplicationDevelopers.pdf.
- [7] Geant4 Collaboration. Geant4 User's Guide for Application Developers Appendix: Material Names. Accessed: November 20, 2024. 2024. URL: https://geant4-userdoc.web.cern.ch/UsersGuides/ForApplicationDeveloper/html/Appendix/materialNames.html.
- [8] LAGO Collaboration. ARTI: Atmospheric Radiation Transfer and Instrumentation. Accessed: November 9, 2024. 2024. URL: https://github.com/lagoproject/arti.
- [9] Paul M Davis and Malcolm JS Johnston. "Localized geomagnetic field changes near active faults in California 1974–1980". In: *Journal of Geophysical Research: Solid Earth* 88.B11 (1983), pp. 9452–9460.
- [10] Inc. Docker. What is Docker? Accessed: November 23, 2024. 2024. URL: https://docs.docker.com/get-started/docker-overview/.
- [11] Pablo Andrés Buitrón Espinoza. Code snippet in rungo.sh, line 12, from masterthesis repository. Accessed: 2024-11-10. 2023. URL: https://github.com/pablobuitron/masterthesis/blob/master/rungo.sh#L12.
- [12] Pablo Andrés Buitrón Espinoza. masterthesis. Accessed: 2024-11-10. 2023. URL: https://github.com/pablobuitron/masterthesis.

- [13] Yongxin Gao et al. "Induced electromagnetic field by seismic waves in Earth's magnetic field". In: *Journal of Geophysical Research: Solid Earth* 119.7 (2014), pp. 5651–5685.
- [14] Google Cloud. Google Kubernetes Engine Documentation. Available at: https://cloud.google.com/kubernetes-engine/docs/ [Accessed: November 9, 2024]. Google Cloud. 2024.
- [15] Peter KF Grieder. "Extensive air showers: high energy phenomena and astrophysical aspects-a tutorial, reference manual and data book". In: (2010).
- [16] D. Heck and T. Pierog. Extensive Air Shower Simulation with CORSIKA: A User's Guide. Accessed: November 24, 2024. 2024. URL: https://www.iap.kit.edu/corsika/downloads/CORSIKA\_GUIDE7.7550.pdf.
- [17] D. Heck et al. CORSIKA: A Monte Carlo Code to Simulate Extensive Air Showers. Tech. rep. FZKA 6019. Accessed: November 23, 2024. Forschungszentrum Karlsruhe, 1998. URL: https://web.iap.kit.edu/corsika/physics\_description/corsika\_phys.pdf.
- [18] W. Heitler. *The Quantum Theory of Radiation*. 1st. Oxford: Oxford University Press, 1954.
- [19] Piotr Homola et al. "Observation of large scale precursor correlations between cosmic rays and earthquakes with a periodicity similar to the solar cycle". In: *Journal of Atmospheric and Solar-Terrestrial Physics* 247 (2023), p. 106068.
- [20] jamalpen. Dockerfile for CORSIKA Simulations. Accessed: November 23, 2024. URL: https://github.com/jamalpen/personal\_notes/blob/main/CORSIKA\_simulations/Dockerfile.
- [21] Karl-Heinz Kampert and Alan A Watson. "Extensive air showers and ultra high-energy cosmic rays: a historical review". In: *The European Physical Journal H* 37.3 (2012), pp. 359–412.
- [22] Peter KF. Cosmic Rays at Earth: Researcher's Reference Manual and Data Book. Elsevier, 2001.
- [23] James Peñafiel L. CORSIKA Docker Image. Accessed: November 23, 2024. 2024. URL: https://hub.docker.com/r/jpenafiell/corsika/tags.
- [24] James Peñafiel L. Dockerfile for the master\_tesis Project. Accessed: November 23, 2024. 2024. URL: https://github.com/jamalpen/master\_tesis/blob/g4prueba1/G4\_Container/Dockerfile.
- [25] James Peñafiel L. Geant4 v10.7.3 Docker Image. Accessed: November 23, 2024. URL: https://hub.docker.com/r/jpenafiell/geant4-v10.7.3/tags.
- [26] LAGO Collaboration. LAGO Project Latin American Giant Observatory. Accessed: 2024-12-01. 2024. URL: https://lagoproject.net/index.html.
- [27] Antoine Letessier-Selvon and Todor Stanev. "Ultrahigh energy cosmic rays". In: Reviews of modern physics 83.3 (2011), pp. 907–942.
- [28] David A Lockner, Malcolm JS Johnston, and James D Byerlee. "A mechanism to explain the generation of earthquake lights". In: *Nature* 302.5903 (1983), pp. 28–33.

- [29] F Masci, P Palangio, and M Di Persio. "Magnetic anomalies possibly linked to local low seismicity". In: *Natural Hazards and Earth System Sciences* 9.5 (2009), pp. 1567–1572.
- [30] J. Matthews. "A Heitler model of extensive air showers". In: Astroparticle Physics 22.5 (2005), pp. 387-397. DOI: 10.1016/j.astropartphys.2004. 09.003. URL: https://www.iap.kit.edu/corsika/downloads/CORSIKA\_GUIDE7.7550.pdf.
- [31] George W Moore. "Magnetic disturbances preceding the 1964 Alaska earthquake". In: *Nature* 203.4944 (1964), pp. 508–509.
- [32] AL Morozova, MI Pudovkin, and TV Barliaeva. "Variations of the cosmic ray fluxes as a possible earthquake precursor". In: *Physics and Chemistry of the Earth, Part A: Solid Earth and Geodesy* 25.3 (2000), pp. 321–324.
- [33] Kenzo Nakamura. "Review of particle physics". In: Journal of Physics G: Nuclear and Particle Physics 37.7 A (2010).
- [34] James Peñafiel. github repository. Accessed: 2024-11-10. 2023. URL: https://github.com/jamalpen/master\_tesis.
- [35] Christian Sarmiento-Cano et al. "The ARTI framework: cosmic rays atmospheric background simulations". In: *The European Physical Journal C* 82.11 (2022). Referencing Fig. 4, p. 1019.
- [36] Todor Stanev. "Cosmic rays in the atmosphere". In: *High Energy Cosmic Rays* (2021).
- [37] Jianfeng Su and Hai Chen. "Study on the mechanism of atmospheric electric field anomalies before earthquakes". In: *Results in Geophysical Sciences* 15 (2023), p. 100060.
- [38] EM Takla et al. "Geomagnetic variations possibly associated with the Pisco earthquake on 15 August 2007, Peru". In: *Tectonophysics* 524 (2012), pp. 29–36.